universität wien

BACHELORARBEIT / BACHELOR'S THESIS

Titel der Bachelorarbeit / Title of the Bachelor's Thesis

„Propagating Spin-Wave Spectroscopy at the Macroscale and Nanoscale“

verfasst von / submitted by

Artemis Stamos, BSc

angestrebter akademischer Grad / in partial fulfilment of the requirements for the degree of

Bachelor of Science (BSc)

Wien, 2025 / Vienna, 2025

Studienkennzahl lt. Studienblatt / degree programme code as it appears on the student record sheet:	UA 033 676
Studienrichtung lt. Studienblatt / degree programme as it appears on the student record sheet:	Bachelorstudium Physik
Betreut von / Supervisor:	Univ.-Prof. Dr. habil. Andrii Chumak
Mitbetreut von / Co-Supervisor:	Kristýna Davídková, M.Eng.

Acknowledgements

I would like to express my deep appreciation to my supervisors, Univ.-Prof. Dr. habil. Andrii Chumak and Kristýna Davídková, M.Eng., for guiding me throughout the research for this thesis. I am beyond grateful as their valuable advice, patience, and dedication were of great benefit to the present study.

I want to extend my sincere acknowledgment to the Universität Wien for giving me the opportunity to pursue my academic studies.

Finally, I am thankful for the support and encouragement from my family, fellow students, and friends.

Declaration of Authorship

I hereby declare that I have independently and without the use of sources other than those indicated, completed the present work. All passages taken literally or paraphrased from published and unpublished publications are identified as such. The work has not been submitted in the same or similar form as an examination paper to any examiner, either domestically or abroad, for evaluation.

Abstract

The investigation of spin waves has gained increasing attention due to their advantages, including energy efficiency, broad frequency operation, and compatibility with miniaturization, allowing the creation of highly compact components difficult or impossible to achieve with conventional CMOS technology. As a result, spin wave technology presents new opportunities for multifunctional, scalable devices that integrate signal processing, filtering, and power limiting in unprecedented ways.

This thesis focuses on improving the experimental setup for Propagating Spin Wave Spectroscopy (PSWS) by developing a new sample holder optimized for in-plane measurements at the nanoscale and a microscope stage for optical inspection during both in-plane and out-of-plane experiments. The main objective is to calibrate the system for 50 Ω impedance matching between microwave antennas and the VNA, enabling accurate nanoscale antenna impedance reconstruction essential for optimizing antenna performance and spin wave transmission. At the macroscale, the work aims to explore the multi-functionality of spin wave devices acting simultaneously as filters, delay lines, and frequency-selective power limiters through detailed analysis of power transmission spectra, time-domain signals, and spin wave transmission characteristics.

PSWS is performed on a pair of mm long stripline antennas fabricated on a 7.78 µm thick YIG film for macroscale measurements and on 440 µm long GS antennas on an 802 nm thick YIG film for nanoscale measurements.

The results confirmed successful calibration and impedance reconstruction, enabled by the new sample holder, while simultaneously achieving relatively small insertion losses below 15 dBm. Further improvements could be achieved by optimizing antenna geometry, contacting technique, and fabrication processes.

Contents

Introduction

Advancements in the field of magnonics, which studies the transport and processing of information via spin waves, have gained increasing attention as a promising technology to address challenges faced by conventional photonic and electron-based devices [1]. New developments in spin-wave research have showcased the potential of magnonic devices for significant miniaturization down to the nanoscale and beyond what is achievable with electromagnetic wave-based technologies, while offering notable advantages such as energy efficiency, broad high-frequency operation, tunability by applied magnetic fields, innovative approaches to data processing, and the exploration of non-linear processes that remain inaccessible even at the macroscale [1–3]. These advantages offer the opportunity for high-speed computing and more efficient signal/data processing and thus paved the way for a variety of advanced applications of spin wave (SW) technology in magnon transistors in electronics, microwave magnetic devices, and RF components, which will include crucial new functionalities in comparison to electron-based devices [2–4] .

Propagating Spin Wave Spectroscopy (PSWS), in particular, has emerged as a powerful tool for investigating the magnetization dynamics in magnetic materials.

The primary objective of this thesis is to improve the experimental setup for in-plane measurements of propagating spin waves at the nanoscale. This is achieved by modifying the sample holder and designing a custom stage for the microscope to significantly improve the measurement setup.

The technique employed in this thesis to analyze spin wave transmission is Propagating Spin Wave Spectroscopy (PSWS). PSWS is an measurement technique that uses inductive antennas and a Vector Network Analyzer (VNA) to excite and detect spin wave (SW) as they propagate through magnetic materials [4]. With this method, the excitation and propagation of spin waves in a magnetic material can be investigated, enabling the precise characterization of spin wave dispersion, mode structure, and antenna efficiency, which is crucial for the design and optimization of nanoscale magnonic devices. To perform PSWS at the nanoscale, microwave antennas are fabricated by e-beam lithography onto a thin Yttrium Iron Garnet (YIG) film, the magnetic material chosen in this work to conduct the measurements because of its small damping. Picoprobes, an integral part of the sample holder, make contact with these microwave antennas, enabling signal transmission and reflection measurements, as they are connected to the VNA through coaxial cables. For accurate measurement acquisition and successful VNA calibration, all three conducting tips of the picoprobes must simultaneously make reliable contact with the antenna pads. Achieving this was proven challenging with the previous sample holder design. However, the newly developed sample holder overcomes this limitation

by integrating goniometric stages that provide controlled pitch movement, and thus tilt the picoprobes so that all probe tips can make precise contact with the antennas on the sample. Such alignment allows the calibration of the system for a 50 Ω impedance matching between the antennas and the VNA. The successful calibration further permits the reconstruction of the impedance of each antenna separately, which in turn provides the possibility to analyze and optimize the antenna performance, to ultimately achieve improved SW transmission can be achieved.

The stage for the microscope, in turn, is engineered to securely position the microscope at an elevated level, allowing optimal access to the sample during both in-plane and out-of-plane measurements. This arrangement enables the precise alignment of the microscope's ocular over the sample (or in front, depending on the configuration and thus facilitates the use of the optical microscope during contacting the antennas on the sample with the picoprobes.

Through these improvements, this study aims to analyze and improve spin wave transmission, which is crucial for the advancement of spin wave-based technologies.

The present thesis is structured as follows: In **Chapter 1**, the fundamental theoretical concepts related to magnetism and spin waves are introduced. This chapter covers the basics of magnetism, micromagnetic energies, magnetization dynamics, ferromagnetic resonance, spin wave modes and their dispersion relations, as well as introduces the magnetic material Yttrium Iron Garnet (YIG). **Chapter 2** presents the experimental and computational method used throughout the presented work: Propagating Spin Wave Spectroscopy (PSWS). The process of excitation, propagation, and detection of spin waves in a magnetic material using microwave antennas and a Vector Network Analyzer (VNA) is described in detail. This chapter also shows the experimental setup for conducting the measurements and outlines the calibration procedure for the VNA at both the macroscale and the nanoscale. In **Chapter 3**, the design and fabrication processes of two key components developed in the frame of this thesis to improve the experimental setup, the sample holder and the stage for the optical microscope, are described, including the 3D models created in Autodesk Inventor that illustrate these designs before their fabrication. This chapter discusses in detail the specific goals and purposes that motivated the development of these two components. **Chapter 4** presents the experimental results obtained at both macro- and nanoscale. At the macroscale, the ability of spin wave devices to simultaneously operate as power limiters, delay lines, and filters is analyzed in detail, through creating SW transmission and power spectra. At the nanoscale, special attention is paid to the reconstruction of the antenna impedances from the S-parameters measured by the VNA and the evaluation of the SW transmission efficiency. In **Chapter 5**, the experimental findings are interpreted, comparing the experimental results with theoretical models. This chapter also addresses the technical challenges encountered during the study, and presents potential future work to improve the current results. The advantages and prospective impact of integrating spin wave technologies into future advanced information processing systems are also discussed. Finally, the **Conclusion** summarizes the main outcomes and reflects on the advancements achieved throughout this study.

1 Theoretical Concepts

This chapter provides an overview of the main theoretical concepts concerning spin waves, including the fundamentals of magnetism, micromagnetic energies, and magnetization dynamics. It also introduces the ferromagnetic resonance condition, spin wave (SW) modes and their dispersion relation, as well as the properties of Yttrium Iron Garnet (YIG) films. These concepts form the basis for understanding the behavior and manipulation of spin waves in magnetic systems. The primary references for the content discussed in this chapter are [5–7].

1.1 Basics of Magnetism

1.1.1 Magnetic and Angular Momentum

The fundamentals of magnetism originate from the intrinsic properties of electrons, specifically their charge, mass, and angular momentum. When an electron moves around the nucleus, it generates a current loop, which then forms a magnetic moment $\boldsymbol{\mu}_\mathrm{L}$. This magnetic moment is proportional to the current and the area enclosed by the electron's orbit. In addition to the magnetic moment, an electron also possesses angular momentum $\boldsymbol{L}$ due to its mass and motion, which points in the opposite direction to the magnetic moment. The ratio of these two quantities, the magneto-mechanical ratio, is a fundamental constant and is central to the quantum theory of magnetism (see Eq. 1.1).

$$\boldsymbol{\mu}_\mathrm{L} = -\frac{\mathrm{e}}{2\mathrm{m_e}}\boldsymbol{L} \tag{1.1}$$

Beyond the orbital contribution, electrons also have an intrinsic angular momentum called spin $\boldsymbol{S}$ (see Eq. 1.2), which is of quantum mechanical origin. The spin generates a magnetic dipole moment, which experiences a torque in the presence of an external magnetic field.

$$\boldsymbol{\mu}_\mathrm{S} = -\frac{\mathrm{e}}{\mathrm{m_e}}\boldsymbol{S} \tag{1.2}$$

The total magnetic moment of an atom results from the vector sum of all individual orbital and spin contributions from its electrons (see Eq. 1.3).

$$\boldsymbol{\mu} = \boldsymbol{\mu}_\mathrm{S} + \boldsymbol{\mu}_\mathrm{L} = -\frac{\mathrm{e}}{2\mathrm{m_e}}(2\boldsymbol{S} + \boldsymbol{L}) \tag{1.3}$$

In solids, magnetic moments interact with each other through various mechanisms (see section 1.2), leading to different degrees of alignment depending on the specific conditions.

This alignment of magnetic moments, either spontaneous as a result of internal interactions or under the influence of an external magnetic field, is the origin of magnetic ordering in materials.

$$\boldsymbol{M} = \sum_i \frac{\boldsymbol{\mu}_i}{\mathrm{V}} \tag{1.4}$$

The macroscopic magnetization, defined as the vector sum of all magnetic moments within a given volume (see Eq. 1.4), serves as a fundamental quantity characterizing the magnetic state of a material. The extent to which the magnetic moments are aligned directly determines the magnitude of the magnetization. Its maximum value is known as the saturation magnetization M_s where all moments are perfectly aligned [8].

Temperature plays a crucial role in magnetic ordering. At higher temperatures, thermal energy induces fluctuations that tend to randomize the orientation of the magnetic moments, thereby reducing the overall magnetization. As the temperature decreases, these thermal fluctuations diminish, allowing the magnetic moments to align more rapidly. The temperature at which a material undergoes a transition from a disordered to an ordered magnetic state is known as the Curie temperature. Below this temperature, spontaneous alignment of magnetic moments can occur, resulting in a stable, ordered magnetic phase.

1.1.2 Magnetic Field

In the context of magnetism, the magnetic field in and around a material is a result of both the externally applied field and the intrinsic response of the material, characterized by its magnetization and influenced by its geometry. It is described by two fundamental quantities: the magnetic field strength $\boldsymbol{H}$ and the magnetic flux density $\boldsymbol{B}$. In a vacuum, these two vectors are directly proportional and point in the same direction, related by the vacuum permeability μ_0, such that:

$$\boldsymbol{B}_\mathrm{ext} = \mu_0 \boldsymbol{H}_\mathrm{ext}\,. \tag{1.5}$$

However, when considering a magnetic material, the relationship between $\boldsymbol{B}$ and $\boldsymbol{H}$ must also account for the magnetization $\boldsymbol{M}$ of the material itself. The internal magnetic flux density is therefore given by the following expression:

$$\boldsymbol{B}_\mathrm{int} = \mu_0(\boldsymbol{H}_\mathrm{ext} + \boldsymbol{M}) \tag{1.6}$$

The magnetization $\boldsymbol{M}$ itself depends on how strongly the material responds to an applied magnetic field, a property quantified by the magnetic susceptibility χ. For linear materials, the magnetization is linearly proportional to the applied field, expressed as $\boldsymbol{M} = \chi \boldsymbol{H}_\mathrm{ext}$, which leads to:

$$\boldsymbol{B}_\mathrm{int} = \mu_0(1+\chi)\boldsymbol{H}_\mathrm{ext} = \mu_0\mu_\mathrm{r}\boldsymbol{H}_\mathrm{ext} \tag{1.7}$$

Hence, χ indicates how much a material will become magnetized in the presence of an external field.

An additional effect to consider is the demagnetization field, $\boldsymbol{H}_\mathrm{d}$, which opposes the magnetization. This field is generated by the induction of magnetic poles at the surface of the material and depends strongly on the shape and size of the sample. The internal field experienced by the material can thus be written as follows:

$$\boldsymbol{H}_\mathrm{int} = \boldsymbol{H}_\mathrm{ext} + \boldsymbol{H}_\mathrm{d} \tag{1.8}$$

where $\boldsymbol{H}_\mathrm{d} = \bar{\boldsymbol{N}}\boldsymbol{M}$ and $\bar{\boldsymbol{N}}$ is the demagnetizing tensor, which is determined by the sample geometry.

For thin magnetic films, the orientation of the magnetization relative to the plane of the film significantly affects the internal field. If the film is magnetized in-plane, the internal field is described by $\boldsymbol{H}_\mathrm{int,IP} = \frac{\boldsymbol{B}_\mathrm{ext}}{\mu_0}$. For out-of-plane magnetization, the demagnetizing field is stronger, and the internal field becomes $\boldsymbol{H}_\mathrm{int,OOP} = \frac{\boldsymbol{B}_\mathrm{ext}}{\mu_0} - M_\mathrm{s}$, where M_s is the saturation magnetization.

1.1.3 Classification of Magnetic Materials

Magnetic materials are broadly classified into five categories: **diamagnetic**, **paramagnetic**, **ferromagnetic**, **antiferromagnetic**, and **ferrimagnetic** [9, 10]. This classification is based on the nature of the individual atomic magnetic moments and the interactions between them, which give rise to distinct magnetic behaviors and ordering phenomena.

Diamagnetic materials are characterized by the absence of permanent magnetic moments in their atoms. When subjected to an external magnetic field, they develop a weak, negative magnetization that opposes the applied field [8]. This effect is generally very weak, and the diamagnetic susceptibility χ is negative and temperature-independent [11].

Paramagnetic materials, in contrast, possess atoms or ions with permanent magnetic moments. However, in the absence of an external magnetic field, these moments are randomly oriented due to thermal agitation, resulting in no net magnetization. When a magnetic field is applied, the moments tend to align with the field, producing a weak, positive magnetization proportional to the field strength. The magnetic susceptibility of paramagnets is positive but small and decreases with increasing temperature, as described by Curie's law.

Ferromagnets exhibit strong interactions that cause their magnetic moments to align parallel to each other even without an external field. This parallel alignment leads to spontaneous magnetization and the formation of magnetic domains, regions where the magnetic moments are uniformly aligned. Ferromagnets display a large, positive susceptibility, and their magnetization can persist even after the external field is removed, a property known as remanence. The temperature above which ferromagnetic order is lost and the material becomes paramagnetic is called the Curie temperature.

In comparison to that, **antiferromagnetic** materials also exhibit long-range magnetic ordering, but in this case, the magnetic moments align antiparallel, resulting in no net macroscopic magnetization. Above a characteristic temperature known as the Néel temperature, antiferromagnets become paramagnetic, as the thermal energy disrupts the

antiparallel alignment.

Ferrimagnetic materials, like Yttrium Iron Garnet (YIG), are similar to antiferromagnets, as the magnetic moments are also aligned antiparallel. However, the moments are unequal in magnitude. Ferrimagnets also form domains, and their overall magnetization is high.

1.2 Micromagnetic Energies

The micromagnetic theory connects the quantum theory (microscopic) and the theory of Maxwell (macroscopic). Using this theory, the total energy of a magnetic system is determined by four main energy contributions: exchange energy, dipolar energy, anisotropy energy, and Zeeman energy. The total energy E_{tot} thus results from the sum of these four energy contributions (see Eq. 1.9), similar to the total effective field $\boldsymbol{H}_{\text{ef}}$, which also results from the sum of the individual components of the magnetic field (see Eq. 1.10). Here ϵ is the energy density. The equilibrium state of the magnetic system is achieved when the total energy is minimized.

$$E_{\text{tot}} = E_{\text{d}} + E_{\text{ex}} + E_{\text{z}} + E_{\text{a}} \tag{1.9}$$

$$\boldsymbol{H}_{\text{ef}} = -\frac{1}{\mu_0}\frac{\partial \epsilon}{\partial \boldsymbol{M}} = \boldsymbol{H}_{\text{d}} + \boldsymbol{H}_{\text{ex}} + \boldsymbol{H}_{\text{ext}} + \boldsymbol{H}_{\text{a}} \tag{1.10}$$

Dipolar Energy

The dipolar energy is a weak, long-range dipolar interaction between individual magnetic moments that depends on the shape of the sample. Mathematically, the dipolar energy and the demagnetizing field are given by:

$$E_{\text{d}} = -\frac{1}{2}\mu_0 \int \int_V \int (\boldsymbol{M} \cdot \boldsymbol{H}_{\text{d}}) \ \text{dV}, \qquad \boldsymbol{H}_{\text{d}} = -\bar{\boldsymbol{N}} \cdot \boldsymbol{M} \tag{1.11}$$

where $\boldsymbol{M}$ is the magnetization, μ_0 is the vacuum permeability, $\boldsymbol{H}_{\text{d}}$ is the demagnetizing field, and $\bar{\boldsymbol{N}}$ is the demagnetization tensor, which depends on the geometry of the sample. The demagnetizing field always acts in a direction that opposes the magnetization, and its strength is highly sensitive to the shape and boundaries of the magnetic body. For example, in thin films magnetized perpendicular to the plane, the demagnetizing field is particularly strong and can significantly reduce the effective internal field.
The dipolar interaction tends to align neighboring magnetic moments antiparallel, thereby minimizing the creation of magnetic charges and reducing the overall dipolar energy. This effect is responsible for the formation of magnetic domains within a material, where regions of uniform magnetization are separated by domain walls. The arrangement of these domains minimizes the total dipolar energy by reducing stray fields outside the material.

The dipolar energy plays a crucial role in understanding the formation and propagation of spin waves at long wavelengths (small wavenumbers), as dipolar interaction leads to characteristic features in the spin wave spectrum, such as distinction into different modes.

Exchange Energy

The exchange energy arises from quantum mechanical interactions between neighboring electron spins. This interaction is described by the Heisenberg Hamiltonian [12, 13]:

$$\mathcal{H} = -2\frac{\mathrm{J}}{\hbar^2}\boldsymbol{S}_1\boldsymbol{S}_2 \tag{1.12}$$

where J is the exchange constant, which describes the coupling between spins, and $\boldsymbol{S_1}, \boldsymbol{S_2}$ are the spin operators of neighboring electrons. The sign and magnitude of J determine the preferred alignment of adjacent spins. Thus the exchange interaction is accountable for the fundamental distinction between ferromagnetic and antiferromagnetic materials: for $\mathrm{J} > 0$ the minimum energy is achieved when all spins are aligned parallel, giving rise to ferromagnetic ordering, while for $\mathrm{J} < 0$, the lowest energy state is realized when neighboring spins are antiparallel, characteristic of antiferromagnetic materials.

The exchange interaction is both strong and isotropic, but, in contrast to dipolar interactions, it acts only over very short distances, typically just between neighboring spins. The exchange energy is responsible for the spontaneous magnetic ordering observed in ferromagnets and antiferromagnets, and thus plays a central role in determining the macroscopic magnetic properties of materials. It is also of great importance in spin wave propagation at small wavelengths.
In the continuum approximation, the exchange energy and the associated effective exchange field can be expressed as:

$$E_{\mathrm{ex}} = A_{\mathrm{ex}} \int\int_V\int \left(\nabla\frac{\boldsymbol{M}}{M_{\mathrm{s}}}\right)^2 \mathrm{dV}, \qquad \boldsymbol{H}_{\mathrm{ex}} = \left(\frac{2\mathrm{A}_{\mathrm{ex}}}{\mu_0 {M_{\mathrm{s}}}^2}\right)\nabla^2\boldsymbol{M} \tag{1.13}$$

where A_{ex} is the exchange constant, $\boldsymbol{M}$ is the magnetization, and M_{s} is the saturation magnetization.

As temperature increases, thermal energy can overcome the exchange interaction, leading to a loss of magnetic order above the Curie temperature in ferromagnets or the Néel temperature in antiferromagnets.

Anisotropy Energy

The anisotropy energy originates from the interaction between the magnetization and the crystal lattice structure of a material. This energy contribution reflects the fact that certain crystallographic directions (easy axes) are energetically favored for the alignment of the magnetization. The origin of this effect is rooted in the symmetry of the crystal lattice, which imposes preferential directions that minimize the total energy of the system.

Mathematically, for a material with uniaxial anisotropy, the anisotropy energy and the effective anisotropy field associated with this energy are given by:

$$E_{\mathrm{a}} = \int \int_V \int \mathrm{K_u} \sin^2(\theta)\ \mathrm{dV} \qquad \boldsymbol{H}_{\mathrm{a}} = \frac{2\mathrm{K_u}}{\mu_0 \boldsymbol{M}_s} \boldsymbol{z} \tag{1.14}$$

where $\mathrm{K_u}$ is the anisotropy constant, θ is the angle between the magnetization vector and the easy axis, and $\boldsymbol{M}_s$ is the saturation magnetization. The direction of $\boldsymbol{z}$ corresponds to the easy axis of the crystal. The magnitude of the anisotropy constant $\mathrm{K_u}$ depends on the specific lattice structure and chemical composition of the material. In materials with high crystalline symmetry, the anisotropy energy can have multiple easy axes.

The energy is minimized when the magnetization aligns with the easy axis ($\theta = 0$), and maximized when it is perpendicular to the easy axis ($\theta = 90°$), which is referred to as the hard axis. In materials with high anisotropy energy, the magnetization remains aligned along the easy axis, while at low energies, the magnetization tends to reorient itself under the applied field.

Zeeman Energy

The Zeeman energy (see Eq.1.15) describes the interaction of the magnetization $\boldsymbol{M}$ with an external magnetic field $\boldsymbol{H}_{\mathrm{ext}}$, favoring an alignment of all individual magnetic moments along the direction of the external field, in order to achieve minimum energy.

$$E_{\mathrm{z}} = -\mu_0 \int \int_V \int (\boldsymbol{M} \cdot \boldsymbol{H}_{\mathrm{ext}})\ \mathrm{dV} \tag{1.15}$$

1.3 Magnetization Dynamics

1.3.1 Torque effect: Landau-Lifshitz-Gilbert (LLG) Equation

The dynamics of magnetization in a magnetic material are fundamentally governed by the torque exerted on the magnetic moments by an external magnetic field. This torque arises from the interaction between a magnetic moment $\boldsymbol{\mu}$ and the magnetic field $\boldsymbol{B}$, expressed as:

$$T = (\boldsymbol{\mu} \times \boldsymbol{B}) = \mu_0(\boldsymbol{\mu} \times \boldsymbol{H}_{\mathrm{ef}}) \tag{1.16}$$

Here, the effective field $\boldsymbol{H}_{\mathrm{ef}}$ does not correspond solely to the externally applied field, but includes all components of the magnetic field (see Eq. 1.10).

The torque can also be written as the time derivative of the angular momentum $\boldsymbol{J}$ of a magnetic system:

$$T = \frac{\partial \boldsymbol{J}}{\partial \mathrm{t}} \tag{1.17}$$

where $\boldsymbol{J}$ is defined as:

$$\boldsymbol{J} = -\frac{\boldsymbol{\mu}}{\gamma} = -\frac{\mathrm{e}}{2\mathrm{m_e}\gamma}(2\boldsymbol{S} + \boldsymbol{L}) \tag{1.18}$$

in which γ is the gyromagnetic ratio, $\boldsymbol{L}$ is the vector sum of orbital angular momentum of all electrons in an atom, $\boldsymbol{S}$ is the vector sum of spin angular momentum, e is the electron charge, and m_e is the elctron mass.

Plugging Eq. 1.17 into Eq. 1.16, yields the torque for a single spin:

$$\frac{\partial \boldsymbol{\mu}}{\partial t} = -\gamma \mu_0 (\boldsymbol{\mu} \times \boldsymbol{H}_{ef}) \tag{1.19}$$

When considering a collection of magnetic moments within a material, the magnetization $\boldsymbol{M}$ can be defined as the vector sum over a given volume, and the torque equation can be translated into the Landau-Lifshitz equation [7, 14]:

$$\frac{\partial \boldsymbol{M}}{\partial t} = -\gamma \mu_0 (\boldsymbol{M} \times \boldsymbol{H}_{ef}) \tag{1.20}$$

The total energy of the system is minimized when the magnetization $\boldsymbol{M}$ aligns with the direction of the effective field. This means that at equilibrium (steady state), the torque vanishes, and the magnetization points along the direction of minimal total energy:

$$\frac{\partial \boldsymbol{M}}{\partial t} = 0 \tag{1.21}$$

However, the Landau-Lifshitz (LL) equation implies that equilibrium is never reached as the magnetization precesses forever around the equilibrium state at the Larmor frequency $\boldsymbol{\omega} = \gamma \mu_0 \boldsymbol{H}_{ef}$ (see Fig. 1.1). On the contrary, real materials exhibit relaxation processes, which cause the magnetization to execute a spiral motion until eventually aligning with the effective field (see Fig.1.1). To account for the energy dissipation and relaxation processes within the material, the Gilbert damping term is introduced, resulting in the Landau-Lifshitz-Gilbert (LLG) equation:

$$\frac{\partial \boldsymbol{M}}{\partial t} = \underbrace{-\gamma_G \mu_0 (\boldsymbol{M} \times \boldsymbol{H}_{ef})}_{\text{Precession around equilibrium}} + \underbrace{\frac{\alpha}{M_s} \left(\boldsymbol{M} \times \frac{\partial \boldsymbol{M}}{\partial t} \right)}_{\text{Damping towards equilibrium}} \tag{1.22}$$

where α is the dimensionless Gilbert damping parameter and γ_G is the gyromagnetic ratio.

The LLG equation describes how the system evolves towards this energy minimum, with the damping term ensuring eventual relaxation to equilibrium. The combined precession-damping mechanism forms the basis for spin wave (SW) propagation in magnetic materials.

1.4 Ferromagnetic Resonance (FMR)

Ferromagnetic Resonance (FMR) arises due to the reaction of the magnetization $\boldsymbol{M}$ in a uniformly magnetized ferromagnetic material to an external magnetic field $\boldsymbol{H}_{ext}$. The FMR frequency corresponds to the frequency at which the magnetization precesses coherently (all magnetic moments in the sample at the same phase and frequency) around the direction of the applied static magnetic field, across the material. The key equation

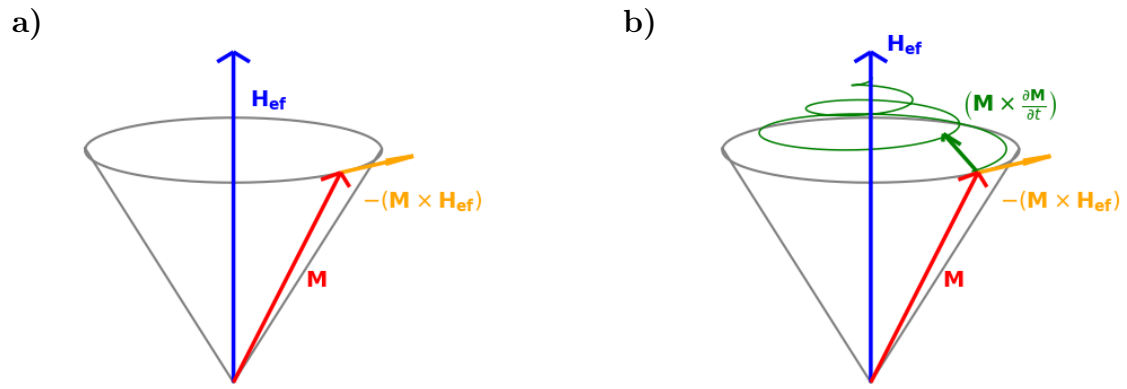

Figure 1.1: Magnetization dynamics. a) Precession of magnetization around the equilibrium state. b) Damping of magnetization towards the equilibrium state.

governing this precessional motion is the LL equation (see section 1.3.1). The resonance condition can be derived using the Landau-Lifshitz equation (see Eq. 1.20). As visible from Equation 1.20, the resonance condition is tunable by varying the external magnetic field, and can thus be used to manipulate the magnetization dynamics of magnetic systems.

Assuming negligible anisotropy and exchange interaction, the effective field $\boldsymbol{H}_{\mathrm{ef}}$ simplifies to the sum of the external field $\boldsymbol{H}_{\mathrm{ext}}$ and the demagnetization field $\mathbf{H}_{\mathrm{d}}$ = - $\bar{\boldsymbol{N}}\boldsymbol{M}$:

$$\boldsymbol{H}_{\mathrm{ef}} = \boldsymbol{H}_{\mathrm{ext}} + \boldsymbol{H}_{\mathrm{d}} \tag{1.23}$$

Under these conditions, the FMR frequency [6], is given by:

$$\boldsymbol{\omega}_{\mathrm{FMR}} = \gamma\sqrt{\left(\boldsymbol{B}_{\mathrm{ext}} + (\boldsymbol{N}_{\mathrm{x}} - \boldsymbol{N}_{\mathrm{z}})\mu_0 M_{\mathrm{s}}\right)\left(\boldsymbol{B}_{\mathrm{ext}} + (\boldsymbol{N}_{\mathrm{y}} - \boldsymbol{N}_{\mathrm{z}})\mu_0 M_{\mathrm{s}}\right)} \tag{1.24}$$

For a thin ferromagnetic film magnetized in-plane, the FMR frequency can be calculated using a simplified equation, the Kittel formula [6]:

$$\boldsymbol{\omega}_{\mathrm{FMR}} = \gamma\sqrt{\boldsymbol{B}_{\mathrm{ext}}\left(\boldsymbol{B}_{\mathrm{ext}} + \mu_0 M_{\mathrm{s}}\right)} \tag{1.25}$$

The uniform precession mode, described by the FMR, is equivalent to a spin wave with infinite wavelength and consequently a wavevector $\boldsymbol{k}$=0. The oscillation is spatially uniform throughout the sample. Spin waves, in contrast, represent non-uniform precessions with a finite wavevector $\boldsymbol{k}$. The FMR frequency is thus a specific case of the spin wave spectrum at $\boldsymbol{k}$=0.

FMR is a powerful technique to characterize magnetic material, as it provides information about the material properties of the magnetic sample, such as the damping constant and the gyromagnetic ratio.

1.5 Spin Waves

Spin waves are characterized as a collective oscillation of magnetic moments in a magnetically ordered medium. A spin wave arises from the excitation of a single magnetic moment, causing it to precess around the equilibrium state. The precession of one spin stimulates the neighboring spins through interactions, causing them to precess as well. As neighboring magnetic moments are not precessing in phase with each other, a wave-like pattern is created, the spin wave (SW), which propagates through the medium with the wavevector pointing in the direction of propagation (see Fig. 1.2) [15]. A SW is spatially and temporally varying, making it distinct from the uniform precession mode observed in FMR.

The quantized unit of a spin wave is called a magnon, a quasiparticle that carries both energy and angular momentum. The study of spin waves forms the basis of the field known as Magnonics [15].

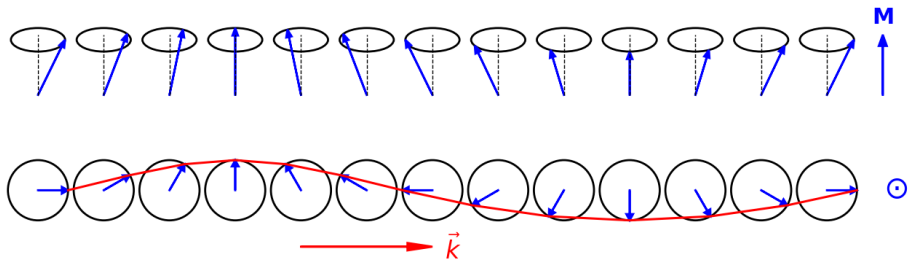

Figure 1.2: Schematic representation of a propagating spin wave, side view (top row), top view (bottom row) (inspired by [16]).

SWs possess several key properties that make them promising for future technologies. The behavior of spin waves often enters a nonlinear regime, which is of utmost importance in developing logic circuits and specialized devices such as magnon transistors, power limiters, or a nanometer-sized logic gate [2]. In terms of data processing, spin waves enable complex computations, as they carry information in both their amplitude and phase. Another advantage of SWs is their exceptional energy efficiency in comparison to conventional electronic data transmission and processing techniques. Since they carry information through the collective precession of spins in a magnetic material rather than charge movement, SW propagation occurs with no electron scattering, resulting in no Joule heating [2, 10]. Finally, their wavelengths typically range from mm down to nm, enabling significant device miniaturization by allowing magnetic components and circuits to be scaled down to nanometer sizes. SW frequencies vary accordingly, covering a broad range from MHz up to THz (EU high band), which enables their use in both low-frequency and ultra-high-frequency devices [2, 3, 10].

1.5.1 Dispersion Relation

The dispersion relation of SWs describes how their frequency depends on the wavevector and is fundamental for understanding their propagation in magnetic materials. Unlike electromagnetic waves, it is nonlinear and does not approach zero frequency, which means that the group velocity and phase velocity of spin waves are unequal. The dispersion relation is shaped by two principal interactions between the magnetic moments in a magnetically ordered material, the dipole-dipole interaction and the quantum mechanical exchange interaction, and is consequently determined by the type of interaction that dominates in the given wavelength range [17]. As a result, the dispersion relation is divided into three regimes depending on the dominant interaction: dipolar, dipolar-exchange, and exchange [15].

As the exchange interaction strives to maintain parallel alignment between the magnetic moments, the exchange energy increases when the angle between adjacent moments is larger. The exchange interaction dominates at short wavelengths, at approximately $\boldsymbol{\lambda} \leq 200\,\text{nm}$ and $\boldsymbol{k} \geq 10^5\,\text{cm}^{-1}$ (see Fig.1.3) [15].

In contrast, the long-range dipolar interaction dominates when the tilting angle between neighboring spins is small, because exchange interactions don't have an effect anymore. The dipolar interaction becomes significant at long wavelengths, typically $\boldsymbol{\lambda} \geq 1\,\mu\text{m}$ and $\boldsymbol{k} \leq 10^4\,\text{cm}^{-1}$ (see Fig.1.3) [15].

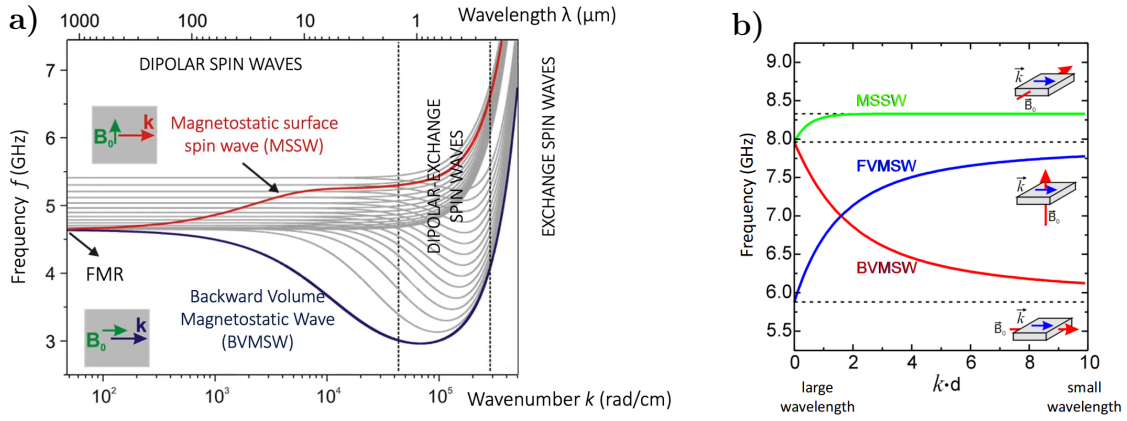

Figure 1.3: a) Spin wave dispersion relation: dipolar-exchange spin-wave dispersion (reprinted from [18]). b) Spin wave modes (reprinted from [19]).

The mathematical description of the three regimes is captured by several key equations:

The Kittel formula (see Eq. 1.25), which, as mentioned before (see section 1.4), can be used to calculate the fmr frequency in thin films magnetized in plane.

The Herring-Kittel formula extends the Kittel formula by including the effect of finite wavevectors, specifically incorporating the exchange interaction, which becomes significant at short wavelengths $\boldsymbol{\lambda}$ (large wavevectors $\boldsymbol{k}$):

$$\boldsymbol{\omega} = \gamma \sqrt{\left(\boldsymbol{B}_{\text{ext}} + \frac{2\mathrm{A}_{\text{ex}}}{\boldsymbol{M}_s}(\boldsymbol{k}_n)^2\right)\left(\boldsymbol{B}_{\text{ext}} + \frac{2\mathrm{A}_{\text{ex}}}{\boldsymbol{M}_s}(\boldsymbol{k}_n)^2 + \mu_0 \boldsymbol{M}_s \sin^2(\theta)\right)} \tag{1.26}$$

Here, A_{ex} is the exchange constant, $\boldsymbol{k}_n$ is the quantized wavevector component normal to the plane of the magnetic film (in direction of the film thickness), and θ is the angle between the magnetization and the wavevector.

The frequencies of Perpendicular Standing Spin Waves (PSSW) are described by the Herring-Kittel formula. PSSW are quantized spin wave modes that form in thin films due to boundary conditions at the surfaces. In PSWS, the wavevector has a component perpendicular to the film plane, leading to standing wave patterns across the film thickness. These modes are observed at higher frequencies than the FMR mode and are sensitive to the exchange interaction.

The most general description of the spin-wave dispersion relation, used in PSWS, is provided by the Kalinikos-Slavin model [20]:

$$\boldsymbol{\omega} = \gamma \sqrt{\left(\boldsymbol{B}_{\text{ext}} + \frac{2\mathrm{A}_{\text{ex}}}{\boldsymbol{M}_s}(\boldsymbol{k})^2\right)\left(\boldsymbol{B}_{\text{ext}} + \frac{2\mathrm{A}_{\text{ex}}}{\boldsymbol{M}_s}(\boldsymbol{k})^2 + \mu_0 \boldsymbol{M}_s \boldsymbol{F}_n\right)} \tag{1.27}$$

where $\boldsymbol{F}_n$ is a function that encapsulates the dipolar interaction and depends on the geometry of the film and the mode profile:

$$\boldsymbol{F}_n = \sin^2(\theta) + P_{\text{n}}\left[\cos(2\theta) + \sin^2(\theta)\sin^2(\varphi)\left(1 + \frac{\mu_0 \boldsymbol{M}_s (1 - P_{\text{n}})}{\boldsymbol{B}_{\text{ext}} + \frac{2A_{\text{ex}}}{\boldsymbol{M}_s}\left(\boldsymbol{k}_{\text{t}}^2 + \left(\frac{n\pi}{d}\right)^2\right)^2}\right)\right]. \tag{1.28}$$

Here, P_n describes the pinning conditions of spin waves, which correspond to the boundary conditions at the surfaces of a magnetic material and influence their propagation.

The Kalinikos and Slavin model provides a theoretical description of both the dipole and the exchange spin wave spectrum in ferromagnetic thin films [20], but becomes inaccurate in the intermediate region where dipole and exchange interactions mix. The model was derived using the classical perturbation theory and incorporates mixed exchange boundary conditions and accommodates any orientation of the bias magnetic field [20].

SW Modes

The shape of the dispersion curve is influenced not only by the regime but also by the SW mode (see Fig.1.3). Depending on the orientation of the external magnetic field relative to the direction of propagation $\vec{k}$, one can distinguish between three characteristic SW modes: Damon-Eshbach (DE), Backward Volume (BV), and Forward Volume (FV) modes. The distinction between these modes is crucial, as they exhibit different dispersion relations, as well as different group velocities (see Fig.1.3) [15].

In the DE mode, also known as Magnetostatic Surface Spin Waves (MSSW) mode, the external magnetic field $\boldsymbol{B}_{\text{ext}}$ is applied in the plane of the sample and oriented perpendicular to the direction of spin-wave propagation $\boldsymbol{k}$. This configuration supports

spin waves that are localized near the surfaces of the film of thickness d. For the dipolar regime, the dispersion relation for the DE mode is given by:

$$f_{\mathrm{DE}} = \frac{\gamma}{2\pi}\sqrt{\left(\boldsymbol{B}_{\mathrm{ext}} + \frac{\mu_0 \boldsymbol{M}_s}{2}\right)^2 - \left(\frac{\mu_0 \boldsymbol{M}_s}{2}\right)^2 e^{-2\boldsymbol{k}d}}\,. \tag{1.29}$$

In the dipolar regime (at high $\boldsymbol{\lambda}$) the dispersion relation for Magnetostatic Surface Spin Waves (MSSW) is characterized by a positive slope (see Fig.1.3), indicating that the wave carries energy in the same direction it propagates (phase velocity $\boldsymbol{v}_{\mathrm{ph}}$ and group velocity $\boldsymbol{v}_{\mathrm{gr}}$ point in the same direction).

In the Backward Volume (BV) mode, both the applied magnetic field $\boldsymbol{B}$ and the wavevector $\boldsymbol{k}$ are aligned parallel and lie in the plane of the sample. The Backward Volume Magnetostatic Spin Waves (BVMSW) propagate through the volume of the material, and their frequency in the dipolar regime is described by the following equation:

$$f_{\mathrm{BV}} = \frac{\gamma}{2\pi}\sqrt{\boldsymbol{B}_{\mathrm{ext}}\left[\boldsymbol{B}_{\mathrm{ext}} + \mu_0 \boldsymbol{M}_s\left(\frac{1 - e^{-\boldsymbol{k}d}}{\boldsymbol{k}d}\right)\right]}\,. \tag{1.30}$$

In contrast to the DE mode, the dispersion of Backward Volume Magnetostatic Spin Waves (BVMSW) in the dipolar regime shows a negative slope (see Fig.1.3), which indicates that group and phase velocities point in opposite directions. Consequently, the phase velocity is running in the opposite direction to the direction of propagation of the SW. However, in the exchange regime, at higher wavevectors $\boldsymbol{k}$, both and modes display similar, nearly quadratic dispersion (see Fig. 1.3), reflecting the dominance of the exchange interaction.

In comparison to the other two SW modes, the Forward Volume (FV) mode occurs when the sample is magnetized out of the plane, with the applied magnetic field $\boldsymbol{B}_{\mathrm{ext}}$ perpendicular to the film surface and the wavevector $\boldsymbol{k}$ perpendicular to the field. The dispersion relation for the Forward Volume Magnetostatic Spin Waves (FVMSW) mode is as follows:

$$f_{\mathrm{FV}} = \frac{\gamma}{2\pi}\sqrt{(\boldsymbol{B}_{\mathrm{ext}} - \mu_0 \boldsymbol{M}_s)\left[\boldsymbol{B}_{\mathrm{ext}} - \mu_0 \boldsymbol{M}_s\left(\frac{1 - e^{-\boldsymbol{k}d}}{\boldsymbol{k}d}\right)\right]}\,. \tag{1.31}$$

As indicated by Eqs. 1.29, 1.30, and 1.31, the shape of the spin wave dispersion curves is strongly affected by both the value of the external magnetic field $\boldsymbol{B}_{\mathrm{ext}}$ and the sample thickness d. Variations in either parameter lead to significant changes in the frequency and propagation characteristics of the different spin wave modes.

1.6 Yttrium Iron Garnet (YIG)

Yttrium Iron Garnet (YIG) is a ferrimagnetic insulator widely used in research in the field of magnonics due to its outstanding magnetic properties. Typically grown on gallium-gadolinium garnet (GGG) substrates, YIG features a unique crystal structure composed

of two sublattices: one containing three iron ions and the other containing two. Looking at its chemical compound $Y_3Fe_5O_{12}$, only the five iron ions give rise to the magnetic properties of the material. The total magnetic moment rises solely from the electron spins, as the orbital angular momentum is fully compensated and therefore does not contribute.

A key property that makes YIG particularly favorable for studies in magnonics and application in spin-wave experiments is its extremely low spin-wave damping (low Gilbert damping parameter), attributed to the absence of free electrons. Furthermore, the lack of orbital angular momentum contribution results in weak spin-orbit coupling, which suppresses the conversion of spin-wave energy into photons and minimizes energy dissipation. As a consequence, YIG supports not only more efficient SW excitation, but also propagation over longer distances than most other magnetic materials, with minimal loss and high consistency. [21, 22]

For the measurements presented in this thesis, YIG films were selected as the magnetic material for the analysis of propagating spin waves. In the nanoscale, a YIG sample of thickness $d = 802$ nm was utilized, while in the macroscale, an $d = 7.78$ µm thick YIG film was employed.

2 Experimental and Computational Methods

This chapter describes the experimental and computational methods used to investigate propagating spin waves, including the procedure of exciting, detecting, and measuring spin waves in magnetic films of different thicknesses. The chapter also presents the principles of impedance matching, S-parameter measurements, and calibration techniques for both macro- and nanoscale measurements. Finally, a detailed description of the experimental setup and measurement procedure is provided.

2.1 Propagating Spin Wave Spectroscopy (PSWS)

The method used in this work to analyze the properties of propagating spin waves is Propagating Spin Wave Spectroscopy (PSWS). This experimental technique typically relies on a pair of inductive transducers, positioned onto a magnetic film and connected to a Vector Network Analyzer (VNA). These transducers serve to convert an incoming microwave signal into spin waves and then reconvert this SW signal back into an electrical signal. This conversion occurs because the alternating current in the transducer produces an oscillating magnetic field that acts on the magnetic moments in the magnetic film, aligned by applying an external magnetic field $\boldsymbol{B}_{\text{ext}}$, exerting a torque that makes them start to precess. This precession of the magnetic moments collectively forms a spin wave, which propagates from the excitation transducer to the detection transducer, where it induces a radio frequency voltage, allowing the measurement of SW transmission and related properties. Efficient excitation occurs only when the microwave signal frequency matches the spin wave frequency defined by the dispersion relation, and when the spin wave number aligns with the size and geometry of the transducer [4].

2.1.1 Microwave Antennas

To perform PSWS, one or more pairs of microwave antennas of different lengths are either directly fabricated onto the surface of the magnetic sample (nanoscale case) or are positioned in the vicinity of the magnetic material (macroscale case). One antenna acts as the excitation source, generating spin waves, while another serves as the detector. Electrical contact to these antennas is established using specialized probes known as picoprobes (see Fig. 2.2), which connect the antennas to the ports of the VNA (see section 2.1.2, more in section 2.1.2). When a current is applied to the excitation antenna, it generates a localized oscillating magnetic field that interacts with the magnetic moments in the material, thereby initiating a propagating spin wave. Once excited, the spin wave

travels through the material from the excitation antenna towards the detection antenna, as illustrated in Fig.2.1. The characteristics of the excited spin wave, particularly its wavenumber and wavelength, are strongly influenced by the physical dimensions of the antennas: smaller antennas are capable of exciting spin waves with higher wavenumbers and correspondingly shorter wavelengths.

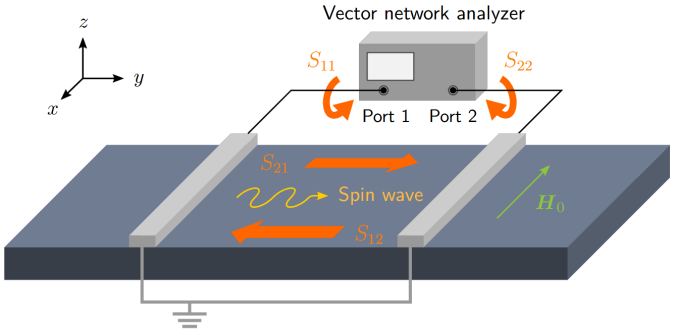

Figure 2.1: Schematic representation of the excitation, propagation, and detection of spin-waves in a magnetic material using a VNA (reprinted from [23]).

There are several types of microwave antenna structures that are commonly used in spin wave spectroscopy, including striplines (rectangular wires), U-shaped ground-signal (GS) antennas, and coplanar waveguide (CPW) antennas. The excitation properties and efficiency of spin wave generation depend significantly on the specific antenna geometry and size. For efficient SW generation and propagation, the wavelength of the spin wave should be larger than the width of the microwave antenna; otherwise, the coupling becomes inefficient, and less energy is transferred to the spin system. [24]

For the measurements presented in this thesis, striplines were employed for macroscale spin wave spectroscopy, while in the nanoscale, measurements were performed using ground-signal (GS) antennas.
As indicated before, for the excitation and detection of spin waves using microwave antennas, a system capable of both generating and measuring microwave frequency signals is essential. This functionality is provided by a Vector Network Analyzer (VNA).

2.1.2 Vector Network Analyzer (VNA)

In this thesis, the R&S ZNA67 VNA is employed, which serves as both the signal source and receiver, operating over a broad frequency range from 10 MHz to 67 GHz [25]. The VNA features two ports that are connected to the Ground-Signal-Ground (GSG) radio frequency (RF) picoprobes via coaxial cables. These picoprobes have three conducting tips that enable precise electrical contact with the antennas (see Fig. 2.2).

When a voltage is applied, the signal generator inside the VNA produces a microwave signal at the set frequency and power level. This signal is sent to one of the two ports and

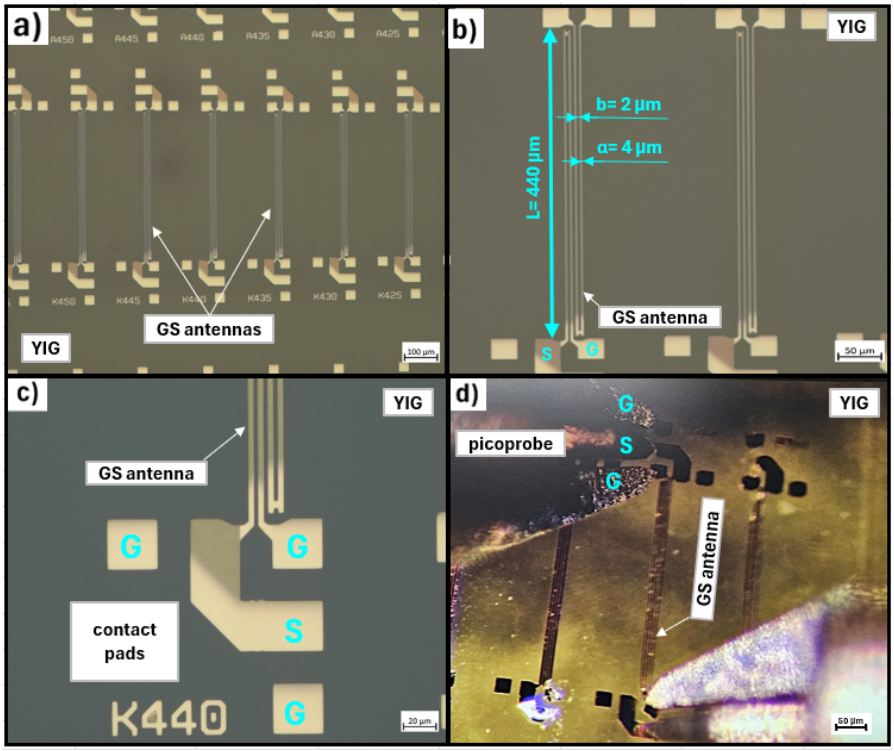

Figure 2.2: Images from the optical microscope. a) Image of the $d = 802\,\text{nm}$ thin YIG film with the micro-antennas fabricated onto it. b) Image of the used $L = 440\,\mu\text{m}$ long GS antenna on the YIG film. The width of the signal (S) and the ground (G) conductor is $a = 3.6\,\mu\text{m}$, and their spacing is $b = 2.4\,\mu\text{m}$. c) Close-up image of the contacting pads of an antenna, with which the picoprobes make contact. d) The three conducting tips of the picoprobes make contact with the contact pads of a GS antenna on the YIG film.

emitted toward the excitation antenna. Part of the signal is reflected at the excitation antenna back to the same port and measured, while the transmitted portion reaches the detection antenna and is measured at the opposite port. By reversing the voltage application to the other port, the roles of excitation and detection are swapped accordingly.

S-parameters

Finally, the VNA measures the four scattering parameters (S-parameters) (see Eq.2.1 and 2.2) that characterize the transmission and reflection of signals at the antennas [26]. These complex parameters contain both amplitude and phase information and are recorded either as amplitude and phase or as real and imaginary components. The measurement process involves first the conversion of the received microwave signals to intermediate frequency (IF) signals. IF is the lower frequency to which a received high-frequency signal is down-converted so that the VNA's analog-to-digital converter (ADC) can process

it, because the ADC is not able to directly translate signals at the original high radio frequencies [27]. This means the IF is the operating frequency at which incoming signals are converted for processing. The IF signals are then digitized, and the VNA's processor calculates the S-parameters from this digital data (see Fig.2.3), which are then displayed on the instrument's screen [27].

$$\Gamma_1 = S_{11} = \frac{b_1}{a_1} \quad \Gamma_2 = S_{22} = \frac{b_2}{a_2} \tag{2.1}$$

$$T_{1\to 2} = S_{21} = \frac{b_2}{a_1} \quad T_{2\to 1} = S_{12} = \frac{b_1}{a_2} \tag{2.2}$$

Specifically, the parameters S_{11} and S_{22} represent the reflection coefficients Γ at each port, indicating the portion of the signal reflected back to the same port, while S_{12} and S_{21} correspond to the transmission coefficients T, describing the signal transmitted from one port to the other (see Fig.2.3). Ideally, the sum of the transmission and the reflection coefficient would equal one (Γ + T = 1) with the transmission being $T = 1$ and the reflection $\Gamma = 0$, indicating total signal transmission without any loss.

Impedance

However, in practical scenarios, losses arise due to signal reflections within the coaxial cables, imperfect contact between the picoprobes and antennas, and impedance mismatches. Impedance Z, measured in ohms (Ω), quantifies the opposition a circuit presents against changes in current [28]. The characteristic impedance of a transmission line is expressed by the ratio of the voltage U and the current I, and is composed of a real part, the resistance R, and an imaginary part, the reactance X (see Eq. 2.3). X is given by the difference of the inductance X_L and the capacitance X_C, where L represent the inductance and C the capacitance.

$$Z = \frac{U}{I} = R + iX = R + i(X_\mathrm{L} - X_\mathrm{C}) = R + i\left(\omega L - \frac{1}{\omega C}\right) \tag{2.3}$$

In ideal lossless lines (Resistance R=0 and Conductance G=0), the characteristic impedance simplifies to:

$$Z = \frac{L}{C} \tag{2.4}$$

Proper impedance matching between the antennas and the VNA is crucial for efficient signal transfer, as mismatches cause signal reflections and reduce the amount of signal transmitted through the system.

In order to minimize systematic errors stemming from cables, connectors, and the measurement setup, and thus achieve more accurate and reliable S-parameter measurements, a thorough calibration of the VNA is crucial. This calibration includes ensuring an impedance match between the antennas Z_1 and the VNA Z_0 (see Fig. 2.3). In the laboratory, 50 Ω is the standard characteristic impedance for such systems, because it

is the mean value between the impedance that minimizes signal attenuation ($\approx 77\ \Omega$) and the characteristic impedance for coaxial cables, which minimizes power loss due to resistive heating ($\approx 30\ \Omega$).

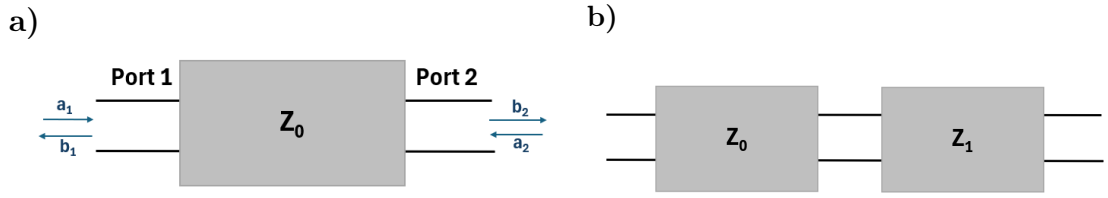

Figure 2.3: a) Schematic representation of a two-port network, illustrating the transmitted and reflected microwave signals (a_1, a_2, b_1, b_1) at each port. Z_0 represents the characteristic impedance of the transmission line. b) Schematic representation of the cascading of two transmission line sections with different characteristic impedances Z_0 and Z_1. Impedance matching $Z_0 = Z_1$ is crucial for minimizing signal reflections.

The four S-parameters measured by the VNA are used to calculate the corresponding impedance values via the following equations, enabling the reconstruction of the system's overall impedance [29]:

$$Z_{11} = Z_0 \frac{(1+S_{11})(1-S_{22}) + S_{12}S_{21}}{(1-S_{11})(1-S_{22}) - S_{12}S_{21}} \tag{2.5}$$

$$Z_{12} = Z_0 \frac{2S_{12}}{(1-S_{11})(1-S_{22}) - S_{12}S_{21}} \tag{2.6}$$

$$Z_{21} = Z_0 \frac{2S_{21}}{(1-S_{11})(1-S_{22}) - S_{12}S_{21}} \tag{2.7}$$

$$Z_{22} = Z_0 \frac{(1-S_{11})(1+S_{22}) + S_{12}S_{21}}{(1-S_{11})(1-S_{22}) - S_{12}S_{21}} \tag{2.8}$$

2.2 Experimental Setup

The experimental setup for in-plane spin wave measurements at the nanoscale consists of the VNA, which is the measurement system, the GMW 3473-70 27,911.00 H-frame Electromagnet, and the new sample holder, developed as part of this thesis (see Fig. 2.4). During the measurements, the sample holder is placed in the poles of the magnet, while the VNA stays connected with the picoprobes via the coaxial cables.

Additionally, a crucial part of the experimental setup is the stage, also designed in the frame of this thesis, on which the microscope is fixed (see Fig. 2.4). The optical microscope is a necessary tool during the process of contacting the antennas with the picoprobes. In order to ensure that the picoprobes indeed make contact with the antennas on the sample, a sourcemeter is employed, which measures the antenna resistance.

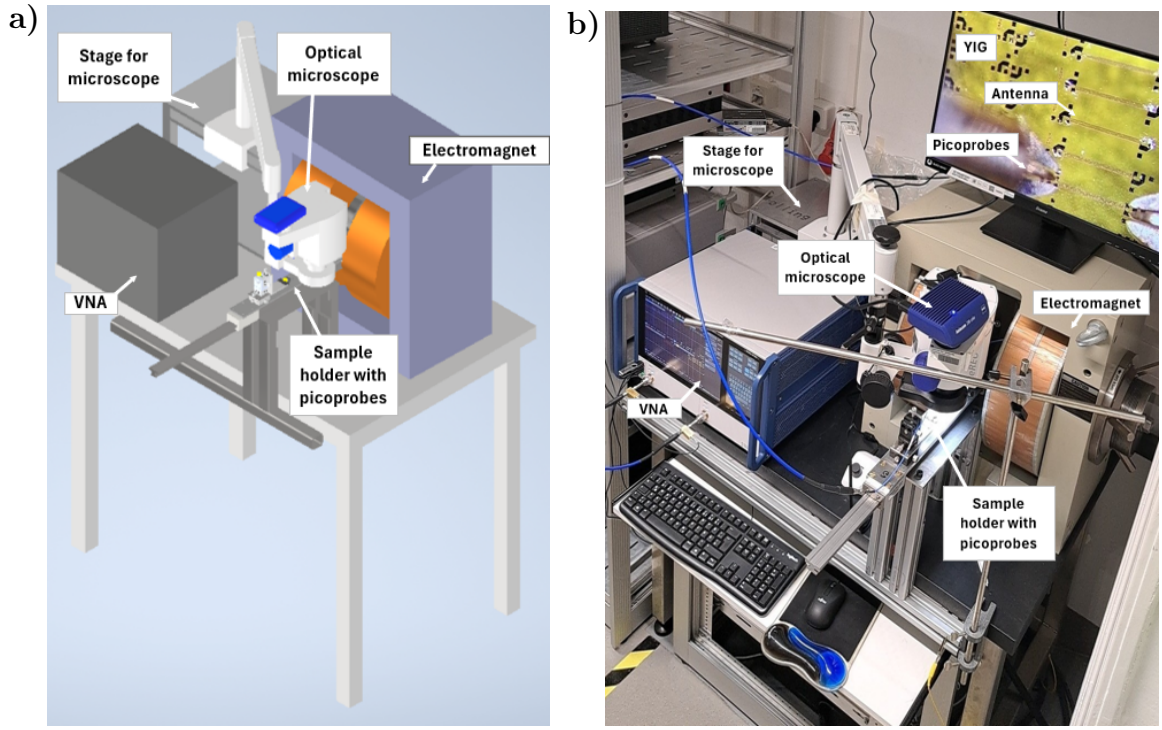

Figure 2.4: Experimental setup for in-plane nanoscale measurements. a) 3D model created in Autodesk Inventor. b) Set up in the laboratory. The optical microscope is fixed on the stage and positioned over the sample on the sample holder.

2.3 Calibration Procedure

Before starting the measurements, the calibration of the VNA is a necessary step both at the nanoscale and the macroscale, to ensure accurate measurement of the S-parameters by removing systematic errors from the test setup. For this purpose, the Open-Short-Load-Through (OSLT) calibration method was employed.

In the 'open' configuration, the signal conductor and ground are separated, resulting in complete reflection of the incident signal ($S_{11} = \frac{A_{out}}{A_{in}} \approx 1$). The 'short' standard directly connects the signal and ground conductors, also producing total reflection ($S_{11} \approx 1$, $S_{21} \approx 0$), but with a phase shift of 90° relative to the open standard. At the 'load' (or 'match') standard, the ground and the signal conductor are connected to a precise 50 Ω impedance, which represents the characteristic impedance of the system. Here, the incident signal is almost entirely absorbed, yielding minimal reflection ($S_{11} \approx 0$) and negligible transmission ($S_{21} \approx -70$ dBm), as energy is dissipated in the load. Finally, the through standard directly connects Port 1 to Port 2, ideally resulting in full transmission ($S_{21} \approx 1$) and minimal reflection ($S_{11} \approx 0$, meaning the outgoing signal closely matches the incoming one.

Even though the calibration method (OSLT) stays the same, the calibration procedure

differs between the macroscale and the nanoscale. At the macroscale, a commercial calibration kit is connected directly to the VNA via coaxial cables. In contrast, nanoscale calibration requires a specialized calibration substrate mounted on the sample holder. The picoprobes, connected to the VNA through coaxial cables, make contact with the individual calibration structures on this substrate, representing the four standards. By comparing the measured signals to the known ideal standards, the VNA computes correction coefficients that remove systematic errors.

3 Design and Fabrication

This chapter describes the design and fabrication of the two mechanical components, the sample holder and a stage for the microscope, which were constructed in the frame of this thesis with the purpose of improving the experimental setup. These components play a vital role in conducting accurate spin wave experiments, especially at the nanoscale.

The new and improved sample holder optimized for in-plane measurements enables calibration for a 50 Ω impedance matching between the antennas and the VNA, which is critical for improving the performance of microwave antennas and ultimately achieving better SW transmission. Effective transmission is crucial in practical applications, as it forms the basis for the development of low-loss, energy-efficient devices for information processing and future magnonic technologies.

The custom-designed stage for the microscope provides a stable base for the microscope, allowing its use in both in-plane and out-of-plane configurations during experiments. A stable microscope is especially important for achieving accurate contact between the picoprobes and the antennas fabricated on the sample, thereby supporting accurate measurements.

3.1 Sample holder

The new and improved sample holder was designed using Autodesk Inventor, a professional CAD software for creating precise 3D mechanical parts and assemblies. The sample holder (see Fig. 3.1) integrates the following three specialized components: First, the 'DT12XYZ - 1/2 " Dovetail Translation Stages' from Thorlabs, which provide precise linear movement along the X, Y, and Z axes. These stages are constructed from brass, a non-magnetic material, ensuring that they do not interfere with the strong magnetic fields applied during measurements. Second, the '1-axis Brass dovetail Goniometer GOH-40A35R' from Optosigma. This goniometric stage allows for the precise tilting of an object about a single axis, enabling a pitch movement. It is also made out of brass, and has an angle range of ±20° and a robust load capacity for mounting of 68.7 N (7 kg). The third and crucial component for exciting and measuring propagating spin waves is picoprobes. The measurements presented in this thesis were performed using the picoprobes by GGB INDUSTRIES INC '40A-GSG-50-P', which have a short conducting tip. These probes are designed for precise, low-noise electrical contact with micro- and nanoscale structures, in this case, the antennas on a sample's surface.

The base of the sample holder consists of a 6 mm thick aluminum plate, chosen for its combination of rigidity, light weight, and non-magnetic properties. On the underside of the plate, two Drylin T-wagons (TW-03-25) from Igus are attached to facilitate the

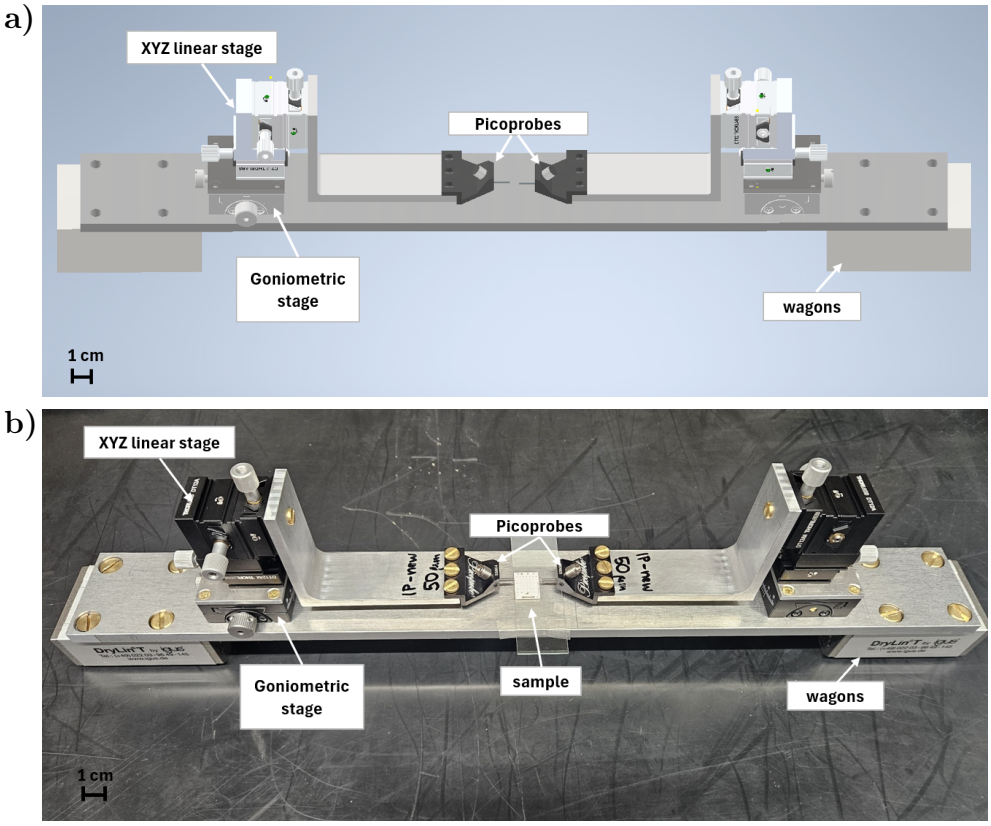

Figure 3.1: Improved sample holder for in-plane measurements. a) 3D model created in Autodesk Inventor, of the newly designed sample holder b) Fabricated and assembled sample holder.

smooth movement of the sample holder on a track. The goniometric stages are screwed to the top of the base plate, one on each side, and the XYZ stages are mounted on top of the goniometers via a thin aluminum mounting plate. The pair of picoprobes is mounted on the edges of two aluminum L-profiles, which are themselves attached to the XYZ translation stages. Two sets of L-profiles of different lengths were designed to accommodate the new sample holder's compatibility not only with the picoprobes '40A-GSG-50-P', which were used in the present measurements and feature short conducting tips, but also with models that have longer tips, such as the 'P-24-5995-A', also from GGB INDUSTRIES INC. The sample (or the calibration substrate) is placed in the middle of the sample holder, where the tips of the picoprobes almost touch. All custom-fabricated metal components are made from aluminum to further ensure that the sample holder remains non-magnetic. Brass screws are used throughout the assembly for the same reason. It is crucial that all parts are made out of a non-magnetic material so they do not interact with or distort external magnetic fields. When the sample holder is inserted into a strong magnetic field, any magnetic components could become magnetized

or act as a source of stray fields. This would lead to unwanted disturbances in the uniformity and strength of the applied field at the sample position, potentially affecting the accuracy and reliability of the measurements.

The key improvement of this new design lies in the integration of the goniometric stages. This pitch adjustment, provided by the goniometers, is critical for achieving optimal contact between the picoprobes and the microscopic antennas patterned onto the sample surface. The ability to fine-tune the angle of contact enables accurate calibration of the measurement system for 50 Ω impedance matching, which is essential for minimizing signal reflections and losses in high-frequency experiments. Moreover, the calibration is an essential step for reconstructing the antenna impedance. Obtaining detailed antenna impedance information allows for the optimization of antenna performance, thereby enhancing SW transmission.

Once the design was finalized, the individual components were fabricated in the workshop and carefully assembled. The assembly process was performed with attention to detail, particularly in the mounting of the stages and the alignment of the picoprobes. The resulting sample holder is specifically optimized for in-plane measurements. Due to the stacked height of the XYZ and goniometric stages, the holder cannot be positioned sideways between the magnetic poles for out-of-plane configurations. In the context of this thesis, the sample holder is used exclusively for measurements at the nanoscale.

3.2 Stage for the microscope

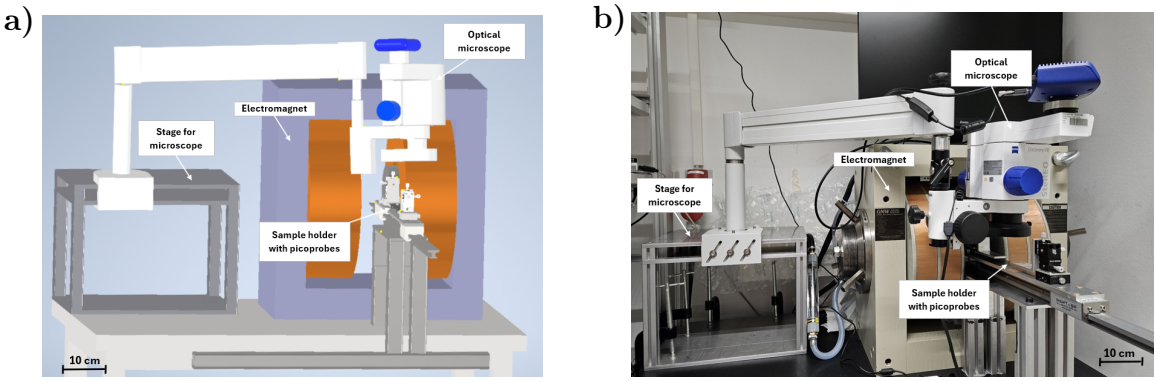

Figure 3.2: Experimental setup incorporating the stage for the microscope a) 3D model created in Autodesk Inventor, showing how the microscope is positioned on the newly designed stage b) Fabricated stage for the microscope and setup in the laboratory.

The stage for the microscope was also designed in Autodesk Inventor and subsequently fabricated in the workshop of the Faculty of Physics of the University of Vienna (see Fig. 3.2). This specific design provides stable and adaptable support for the microscope, used in the experimental setup, while elevating it to a higher level. The main framework

consists of three base plates, each made from 1 cm-thick aluminum. The legs of the holder are 30x30 mm aluminum alloy profile struts supplied by RS PRO, which offer excellent mechanical stability. These struts feature 6 mm nuts, making them ideal for securely attaching the plates and facilitating straightforward assembly with screws.

After fabrication and assembly of the custom parts into a robust structure, the completed stage for the microscope is positioned behind the VNA and clamped firmly to the laboratory table using four heavy-duty clamps to ensure maximum stability. This is especially important given the substantial weight of the microscope, which requires the holder to be securely fixed to prevent any movement or vibration during measurements.

The microscope itself is carefully mounted between the upper and middle plates of the holder, as shown in Figure 3.2. The spacing between these two plates is precisely matched to the maximum opening range of the microscope's clamping mechanism, ensuring a tight and stable fit. Rather than using a single, heavy 5 cm thick aluminum plate to achieve the necessary separation, the design uses two 1 cm plates separated by the aluminum profile legs. This approach not only reduces material usage and overall weight but also maintains the required structural integrity. To further reinforce the assembly and prevent any deformation when the microscope is clamped, an additional section of aluminum profile strut is positioned directly between the plates at the point of maximum load.

The overall design of the stage resembles a compact table, providing a broad and stable base for the microscope (see Fig. 3.2). After the microscope is fixed in place, its arm can be rotated and adjusted vertically, allowing the ocular to be positioned directly above or in front of the sample placed on the sample holder, depending on whether in-plane or out-of-plane measurements are being conducted. With a focal length of 5 cm, the microscope can be precisely focused on the sample surface. The 40 cm length of the stage allows the microscope to be moved laterally and clamped at various positions, making it straightforward to align the ocular with the region of interest on the sample. This flexibility and stability are essential for achieving accurate optical alignment during both in and out-of-plane experiments (see Fig. 2.4).

4 Experimental Results

This chapter presents the experimental results obtained from PSWS experiments using the VNA in two distinct regimes: the macroscale and the nanoscale. At the macroscale, the multi-functionality of SW devices was systematically analyzed, demonstrating their simultaneous capability to operate as filters, delay lines, and power limiters [30]. These measurements highlight the versatility and potential integration of such devices for advanced signal processing applications [4].

In parallel, nanoscale experiments focused on the excitation and detection of spin waves using antennas fabricated by e-beam lithography. Here, special attention was given to SW excitation efficiency of the employed antennas, as well as to the reconstruction of their impedance, which is a crucial aspect for optimizing the performance of the antennas.

4.1 PSWS at the Macroscale

Focusing first on the macroscale experiments, the SW transmission at the macroscale was analyzed on a YIG sample of thickness $d = 7.78\,\mu\text{m}$, with stripline antennas of length $L = 13\,\text{mm}$ and separated by a distance $D = 17.5$ mm from each other, fabricated onto it.

For both the DE and BV modes, three series of measurements were performed. The first series comprised magnetic field sweeps, where the external magnetic field $\boldsymbol{B}_{\text{ext}}$ was varied from 0 to 275 mT in increments of approximately 25 mT at a constant microwave input power of 0 dBm. In the second series, a power sweep was conducted over a range of -80 dBm to 20 dBm in 5 dBm steps, while the magnetic field was maintained at approximately 90 mT. The third series was again a power sweep, but at a lower magnetic field value of around 12 mT. For all measurements, the VNA settings were kept constant at the following parameters: bandwidth of 1 kHz, and no averaging.

The purpose of these measurements is to investigate the multi-functionality of SW devices, specifically the possibility for a single device architecture to function simultaneously as a frequency-selective power limiter, a delay line, and an RF filter [30]. The integration of spin wave technology in CMOS-compatible processes could be a key step towards device miniaturization, ultimately enabling equivalent or enhanced multifunctional performance in nanoscale devices that could overcome the scaling limitations of conventional CMOS electronics [31, 32].

4.1.1 SW transmisssion

Figure 4.1 depicts the SW transmission spectra at frequency ranges around 4 GHz and 8 GHz, which were constructed from the raw data measured with the VNA for

both in-plane fundamental modes, DE and BV. The peaks in the spectra correspond to the frequency at which a spin wave was efficiently excited and transmitted through the magnetic material from the excitation antenna to the detection antenna. As the magnitude of the external magnetic field increases, the resonance peaks are observed to shift to higher frequencies.

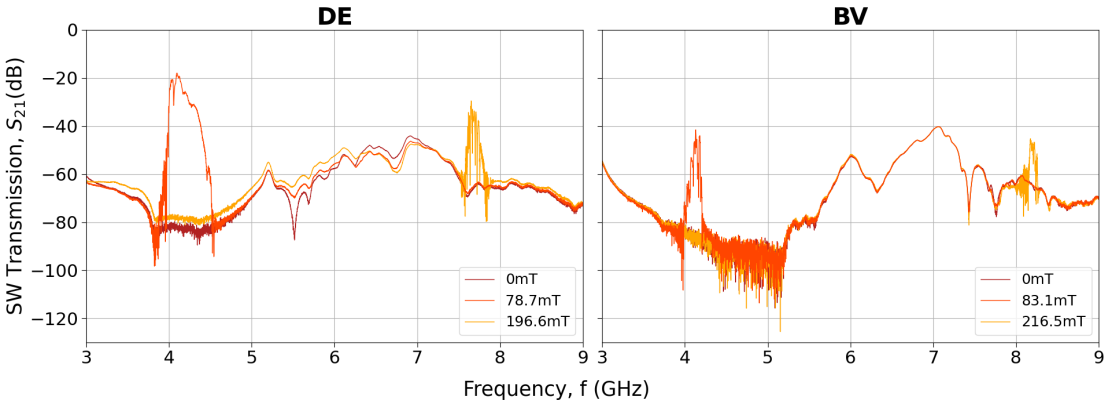

Figure 4.1: Transmitted S_{21} SW signal measured for the DE mode (left pannel) and the BV mode (right panel) at frequency ranges around 4 GHz and 8 GHz and at an input power of 0 dBm using a 7.78 µm thick YIG film

4.1.2 SW dispersion relation and antenna excitation efficiency

Further insight is provided by Figure 4.2, which presents the SW dispersion relation alongside the antenna excitation efficiency J_{exc} (cyan curve), and the group velocity v_{g} (red curve) next to the spin wave transmission S_{21} around a frequency of 4 GHz. The group velocity v_{g} of the SW can be calculated from the derivative of the dispersion relation: $v_{\text{g}} = \frac{2\pi\partial f}{\partial k}$. The dispersion relation for the dipolar regime (black curve) was reconstructed using Equation 1.29 for the DE mode and Equation 1.30 for the BV mode, as well as following input parameters: gyromagnetic ratio $\frac{\gamma}{2\pi} = 28\frac{\text{GHz}}{\text{T}}$, saturation magnetization $M_{\text{s}} = 140\frac{\text{kA}}{m}$. For the calculation of the excitation efficiency of stripline antennas, the following equation was used:

$$J_{\text{exc}}(k) = \left| \frac{\sin\left(\frac{ka}{2}\right)}{\frac{ka}{2}} \right|^2 \tag{4.1}$$

where a is the conductor's width. For the used antennas $a = 60\,\mu\text{m}$.

As visible in Fig. 4.2, the shape of the dispersion relation depends on the mode. The dispersion relation shows how the spin-wave frequency is related to the wave vector for the given experimental conditions, while the antenna excitation efficiency indicates how effectively the microwave antenna on the sample can excite spin waves. The interplay between the SW dispersion and the antenna excitation efficiency defines the range of

frequencies and wave vectors over which spin waves can be efficiently excited and detected, as visualized by the green-shaded area in Figure 4.2. As indicated by the green band in Fig. 4.2, the peaks in the antenna excitation efficiency spectra are in good correspondence with the peaks in the transmission spectra. This agreement demonstrates that Eqs. 1.29 and 1.30 are ideal to recreate the SW dispersion relation in the dipolar regime.

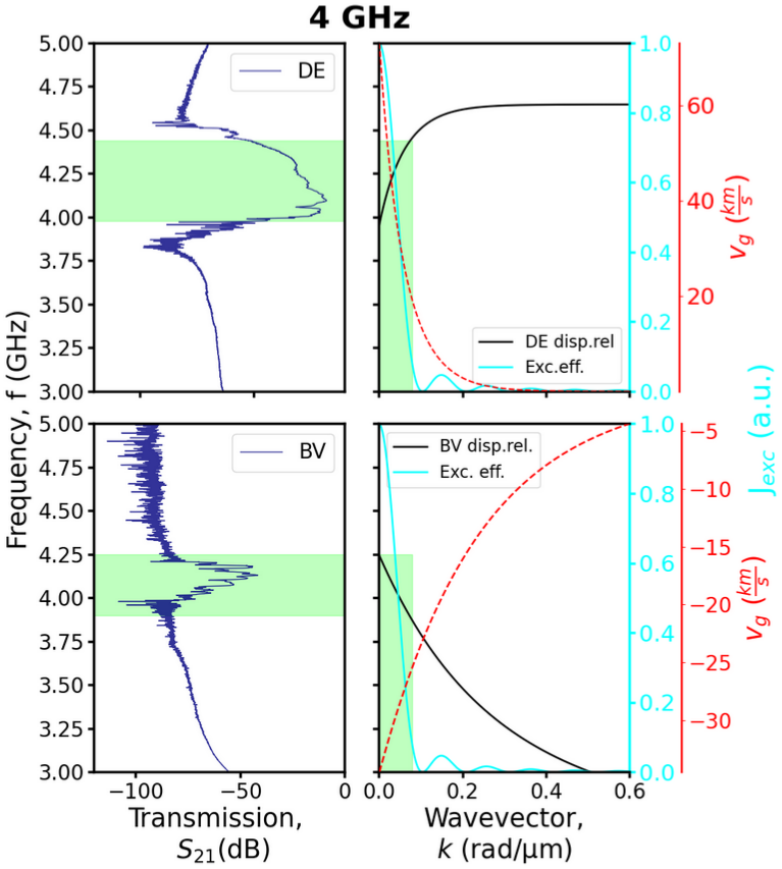

Figure 4.2: (left panels) Spin wave transmission at 4 GHz measured at at an input power of 0 dBm, for the DE mode at 78.7 mT (upper panels) and the BV mode at 83.1 mT (lower panels). (right panels) Calculated dipolar dispersion relation (black curve), antenna excitation efficiency (cyan curve), and group velocity v_g (derivative of dispersion relation, red curve) for a sample of thickness 7.78 µm. The cross-section of the dispersion relation and antenna excitation efficiency is highlighted in green.

4.1.3 Delay line

Applying a Fast Fourier Transform (FFT) to the time-domain signal converts it into the frequency domain [33], which allows for further analysis of the spectral content.

Figure 4.3 depicts the transmitted SW signal both in the time domain (left panels in Fig. 4.3) and in the frequency domain (right panels in Fig. 4.3). The red spectrum in the time-domain plot represents the original signal after the removal of electromagnetic leakage. It corresponds solely to the SW contribution. The frequency domain plots include both the measured raw SW signal (dark blue) and the spectrum after electromagnetic leakage removal (red). The frequency domain data reveal the resonance conditions and bandwidth of the spin-wave modes. An Inverse Fast Fourier Transform (IFFT) can be used to transform the processed frequency-domain data back into the time domain [34]. The depiction of the SW spectrum in the time domain allows an easier separation of the pure spin-wave signal (red) from the original signal (dark blue), which still contains the elmag. leakage.

The ability to switch between the time and frequency domains using the FFT is essential for distinguishing genuine spin wave features from background effects. With this technique, we can isolate, analyze, and interpret the spin wave dynamics with greater clarity and precision. [35].

A key parameter that can be extracted from the time-domain data is the delay time, T. When a microwave signal is converted into a spin wave and sent through a magnetic material, the spin wave travels much slower than electromagnetic waves in conventional transmission lines [32, 36]. This slower propagation causes a measurable time delay (shift) between the excitation and the arrival of the spin-wave packet at the detector [18]. The time value at the peak of the spin wave spectrum in the time domain (see Fig. 4.3) corresponds to the SW delay time T. The magnitude of this delay depends on the distance between the excitation and detection antennas and the group velocity v_g of the spin wave, and thus can be calculated using the two named parameters ($\mathrm{T} = \frac{D}{v_g}$). From the data shown in Figure 4.3, the extracted delay times for a YIG film with thickness 7.78 µm are as follows: $T = 276.56 \pm 43.00$ ns for the DE mode, and $T = 506.00 \pm 31.00$ ns for the BV mode.

Due to the property of SW to propagate at a slower speed, spin wave-based delay lines can be realized, which are functional devices that exploit the propagation characteristics of SW to achieve specific tunable time delays in signal transmission [32].

4.1.4 Filter

Fig. 4.3 also illustrates a distinct approach to background subtraction and signal processing. A filtering technique was applied to the raw data (dark blue) to suppress electromagnetic leakage and isolate the spin-wave signal (red) from background interference. This spectrum was created through manually defining the SW signal without elmag. leakage in the time domain and then transforming it back into the frequency domain via a Fast Fourier Transform (FFT), as shown in the right panel of Fig. 4.3. Alternatively, background subtraction can be performed by subtracting a reference measurement acquired at $\boldsymbol{B} = 0$ mT, where no spin-wave resonance is expected. This method efficiently removes field-independent background contributions, reducing noise. However, it may not fully eliminate electromagnetic leakage between the antennas, which can still obscure the pure spin-wave signal.

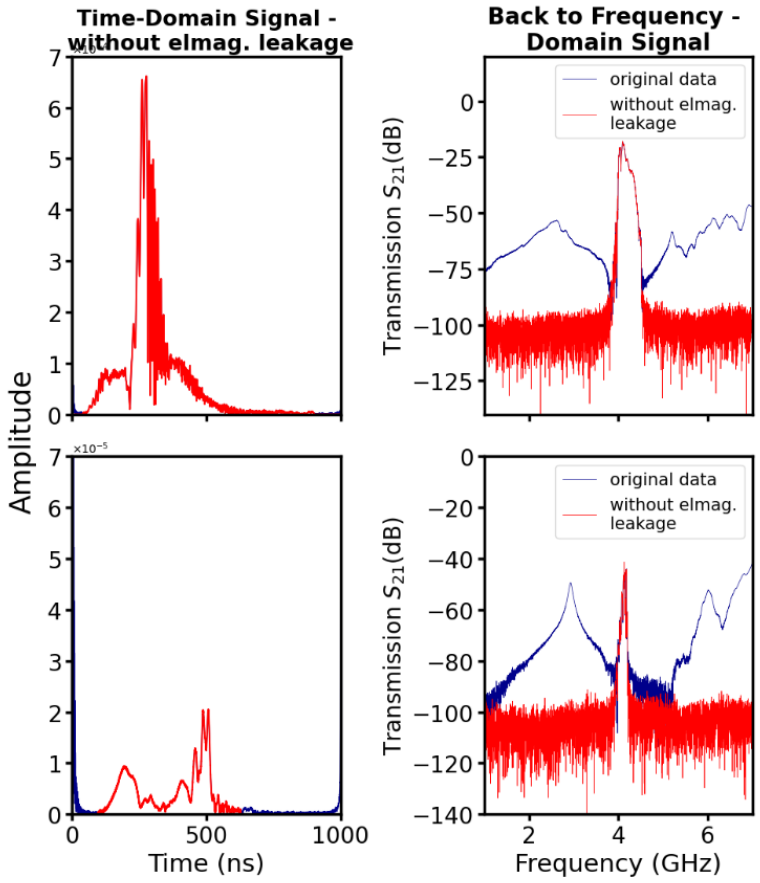

Figure 4.3: (left panels) Time-Domain Signal for a YIG sample of thickness 7.78 µm for the DE mode (upper panels) and the BV mode (lower panels). (right panels) The corresponding frequency domain signal contains the raw data (dark blue) and SW spectrum after elmag. leakage removal.

This ability to allow only a specific frequency band to be transmitted demonstrates the function of SW devices as effective radio frequency (RF) filters [4, 37]. Only those frequencies that match the allowed spin-wave modes in the material are efficiently excited and propagate as spin waves through a magnetic material. The region in Fig. 4.3 where the spectra form a pronounced peak is where the spin-wave device functions as an RF filter. The bandwidth (BW) and the frequency at the maximum define the properties of the filter. In addition to the BW, the dynamic range and insertion loss (IL) are also key parameters for evaluating and designing spin wave devices. These three parameters can be extracted from Fig. 4.3 and are summarized in Table 4.1. The BW, visible in Fig. 4.3 as the width of the peak in the time domain signal, is the frequency range over which the SW device filters the signal. The insertion loss (IL) is the amount of signal that dissipates within the system or gets reflected when it propagates through the device, in this case from the excitation to the detection antenna, while the dynamic range refers

to the difference between the maximum signal value and the noise floor (vertical span).

Mode	B (mT)	IL (dB)	Dynamic range (dB)	BW (MHz)
DE	78.7	17.8 ± 0.1	67.3 ± 2.3	455 ± 35
BV	83.1	41.1 ± 0.1	53.1 ± 1.5	217 ± 1

Table 4.1: Insertion losses IL, dynamic ranges, bandwidths BW extracted from Fig. 4.3 for the in-plane modes DE and BV using a 7.78 µm thik YIG films.

When comparing the extracted data in Table 4.1, the following things were noticed: At around 4 GHz, the DE mode exhibits significantly lower insertion losses compared to the mode, indicating more efficient propagation of DE modes in YIG films at low frequencies. This behavior aligns with theoretical expectations due to the non-reciprocity of DE SWs and the fact that they are surface-localized, thereby benefiting from reduced bulk damping. At these frequencies, DE SWs demonstrate higher group velocities than SWs. An IL of around 40 dBm, like the case for the BV mode, is considered relatively high, as a significant amount of signal is still lost. The dynamic range values are also slightly higher for the DE mode than for the BV mode, indicating robust signal transmission characteristics in the DE mode. This also suggests that the BV mode is more susceptible to noise. However, as this parameter depends on the background and could be improved by reducing the noise through minimizing the elmag. leakage. Finally, concerning the bandwidth, the extracted value for the BV mode is half the value for the DE mode (see Tab. 4.1). While a narrow and sharp peak indicates high-frequency selectivity of the filter, a broader peak supports a wider operational range.

While electromagnetic leakage and other background effects can mask the three critical parameters IL, BW, and dynamic range in the raw data, careful background subtraction and signal processing reveal the true filtering behavior of the spin wave device [38]. Minimizing electromagnetic leakage is therefore crucial, not only for accurate measurements but also for the practical implementation of high-performance spin-wave-based RF filters or logic devices [18]. Effective background and leakage suppression enhance the signal-to-noise ratio and ensure device selectivity and functionality. These techniques are thus essential both for fundamental studies and for the development and optimization of real-world spin wave devices [4, 39, 40].

4.1.5 Power limiter

Figure 4.4 shows the spin wave power transmission spectra for input powers P_{in} ranging from -45 dBm to 10 dBm. The output power was recalculated from the S_{21} transmission parameters, measured by the VNA, using following equation:

$$P_{\text{out}}\,(\text{dBm}) = 20\log_{10}(|S_{21}|)\,(\text{dB}) + P_{\text{in}}\,(\text{dBm}) \tag{4.2}$$

The plotted raw data demonstrate a spin wave-based frequency-selective power limiter (FSL). In this case, the limiting effect of the FSL is based on the propagation of spin

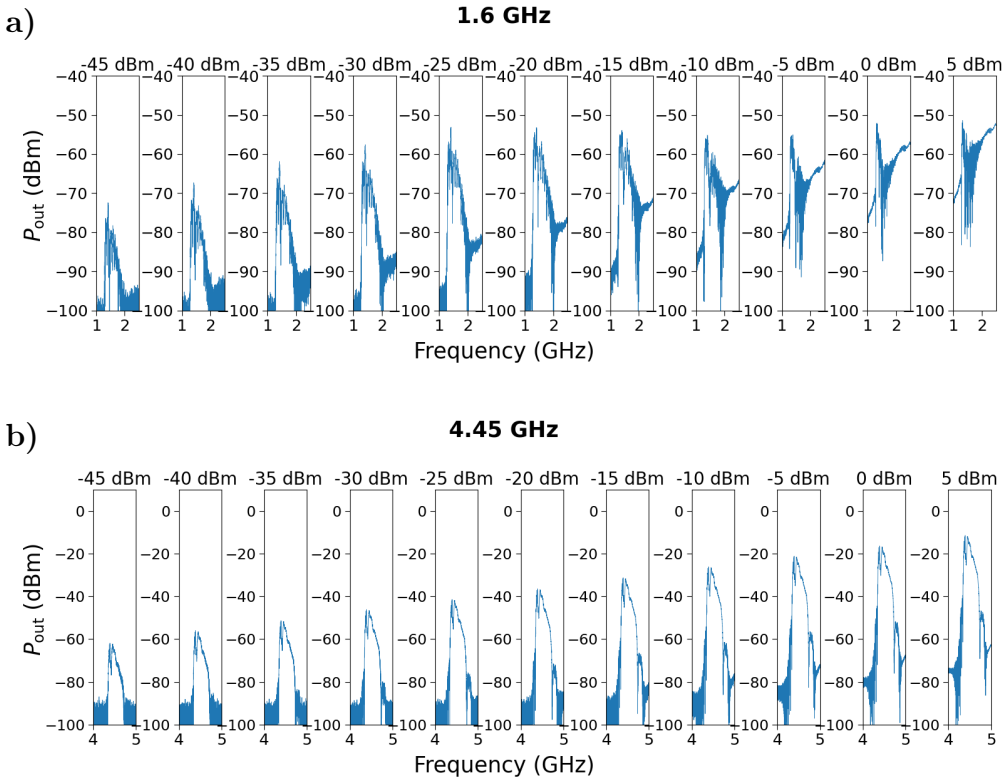

Figure 4.4: Measured SW power transmission for DE mode, for YIG sample thicknesses of 7,78 µm at frequency ranges around a) 1.5 GHz and b) 4.5 GHz for input powers from -45 dBm up to 5 dBm, and at applied magnetic field values of a) 11.8 mT and b) 89.5 mT. Only the raw data (without subtracted background) are plotted.

waves in a magnetic material, instead of using conventional semiconductor limiters. The observed peaks at different input powers correspond to spin-wave resonances, where efficient transmission occurs. The power spectra were created for low frequencies around 1.5 GHz as well as for higher frequencies of around 4.5 GHz. In general, for increasing input power values, the peak in the spectra increases linearly until reaching a certain input power, a threshold P_{th}, after which the spin wave signal either stays constant or even decreases again. The output power, after which the signal stays constant, is called the power limiting level P_{L}.

SW power limiters operate by maintaining a constant output power level once the input power surpasses the threshold. Below the threshold, the device transmits signals with minimal losses. The operation of SW power limiters depends strongly on the SW mode, the applied magnetic field, and the thickness of the magnetic material in which the spin wave propagates. Furthermore, this limiting effect of the output power is based on

multi-magnon scattering phenomena. [4] As input power increases beyond the threshold, multi-magnon scattering occurs, where original magnons are scattered into new magnons with different frequencies and wave vectors. Due to this scattering process, the newly created magnons cannot reach the detection antenna, and energy dissipates, effectively limiting the output power while maintaining frequency selectivity. This power-limiting effect explains why the output power is lower than the input power. [41]

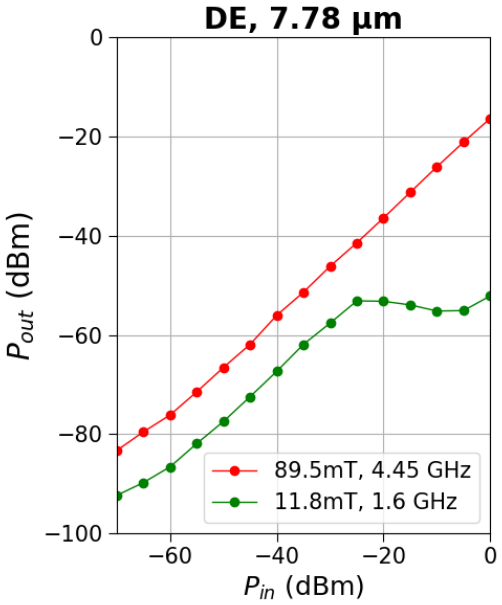

Figure 4.5: Power characteristic extracted from the peaks of the raw data from Figure 4.4 for the DE mode using a 7.78 µm thick YIG sample, at 1.6 GHz and an applied magnetic field of 11.8 mT (green curve) and at 4.45 GHz and an applied magnetic field of 89.5 mT (red curve).

The power characteristic curves, displayed in Fig. 4.5, reveal important information about the power threshold behavior of spin-wave power limiters. The curves were created by extracting the maximum output power from the peaks of the spectra shown in each subplot of Fig. 4.4. The slope and saturation level of the curves reflect how effectively excess input power was converted into scattered magnons.

As seen in Fig. 4.5, the power characteristic curve for the DE mode and at a magnetic field of $\boldsymbol{B} = 11.8$ mT shows a pronounced transition from a linear to a saturated regime, clearly indicating a power threshold at $P_{\mathrm{th}} = -25$ dBm and the corresponding power limiting level at $P_{\mathrm{L}} = -52$ dBm. In contrast, at a high magnetic field, no power threshold and power limiting level can be distinguished as the output power continues to increase linearly at an input power of 0 dBm, suggesting that the threshold occurs above the range explored in these measurements. This observation indicates that, for low magnetic field values, saturation occurs at lower output powers P_{out}, while higher magnitudes shift the threshold to larger input powers. At small magnetic fields, the power limiting effect is

based on 3-magnon scattering, whereas at higher fields, 4-magnon scattering causes the limiting.

4.2 PSWS at the Nanoscale

At the nanoscale, PSWS was carried out on U-shaped GS antennas of length $L = 440\,\mu m$ (see Fig. 2.2). The GS antennas were patterned on a $d = 802\,nm$ thin YIG film. The SW transmission measurements were conducted in the frequency ranges around 4 GHz and 8 GHz and at an input power of -15 dBm for the in-plane modes DE and BV. Additionally, the following parameters were set on the VNA: no averaging, bandwidth 1 kHz, and frequency step size 80 kHz.

The primary aim of these measurements is to test the newly designed sample holder, which incorporates goniometric stages (see Fig. 3.1), and see if, as predicted, it enables the calibration for a 50 Ω impedance matching between the antennas and the VNA. A successful calibration should allow for the reconstruction of the antenna impedances. Consequently, the experiments presented in this section provide an essential basis for investigating and optimizing the microwave antennas to achieve improved SW transmission.

4.2.1 SW transmission

Figure 4.6 shows the measured SW transmission and reflection spectra for the in-plane modes DE and BV. The spectra were constructed from the S-parameters measured by the VNA.

At the peaks in the S_{21} SW transmission spectra of Fig. 4.6, the IL were extracted for both spin wave modes, and summarized in Table 4.2. A low IL value as close as possible to 0 dBm is desirable, as this indicates efficient signal transmission, fewer signal losses due to reflections, and consequently, better spin wave propagation. In the presented experiments, the insertion losses are below 15 dB (see Tab. 4.2), which is already good but still leaves room for further optimization. A comparison of the values in Table 4.2, reveals that for both modes, the IL are smaller around 8 GHz than around 4 GHz. Additionally, the IL for the DE mode are lower than for the BV mode. This is attributed to the nonreciprocity of DE SWs [4].

	4 GHz		8 GHz	
Mode	B (mT)	IL (dB)	B (mT)	IL (dB)
DE	69	10.51 ± 0.10	204	8.20 ± 0.10
BV	87.5	14.84 ± 0.50	220	12.62 ± 0.30

Table 4.2: The applied magnetic fields B and the extracted insertion losses IL for DE and BV modes at 4 GHz and 8 GHz, measured on a 802 nm thin YIG film, using 440 µm long GS antennas. The IL were extracted from the SW transmission spectra (see Fig. 4.6).

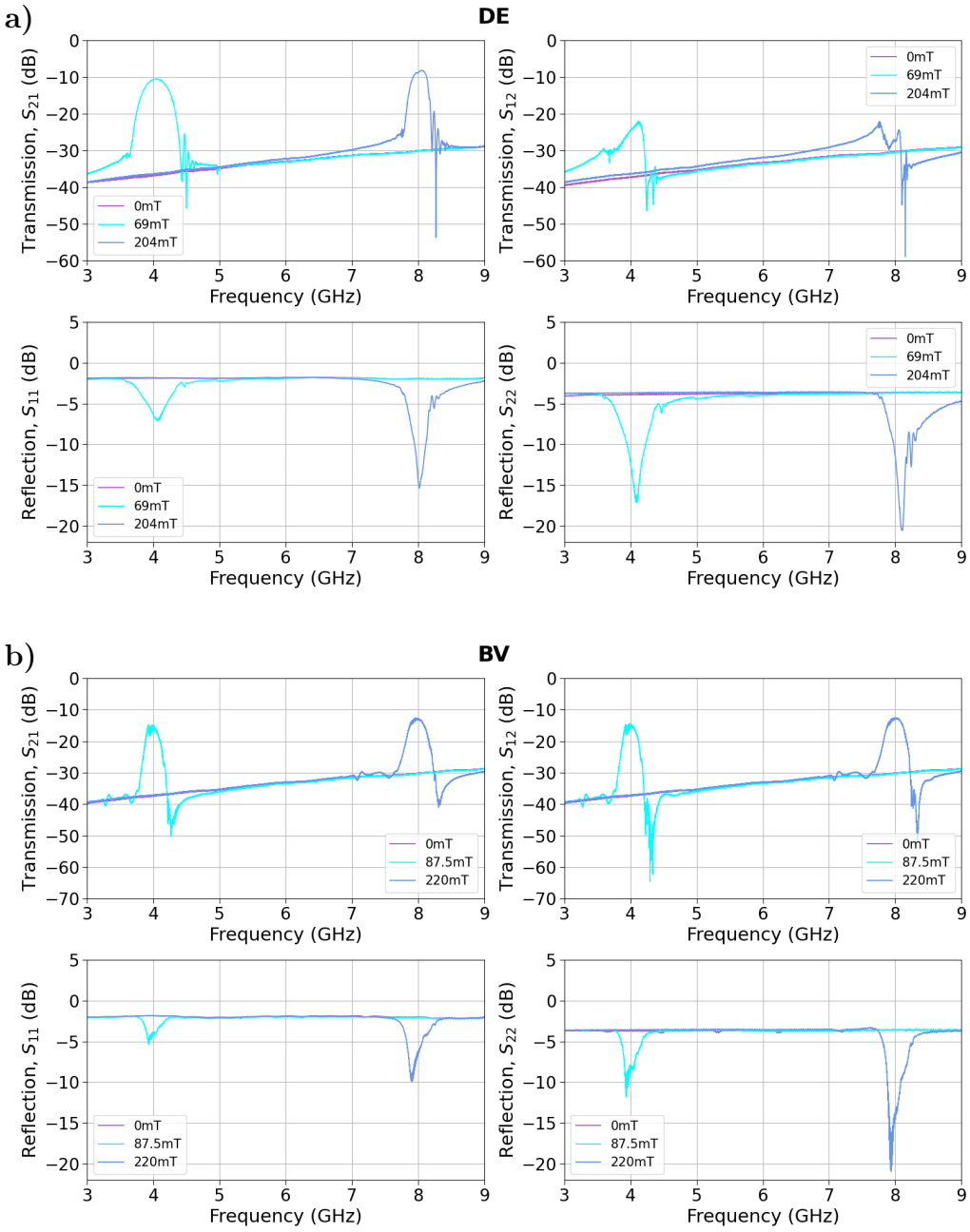

Figure 4.6: Measured S-parameters using 440 µm long GS antennas fabricated on a YIG film of thickness 802 nm at frequency ranges around 4 GHz and 8 GHz, measured at an input power of -15 dBm for a) DE and b) BV modes. The applied magnetic fields are indicated in the legend.

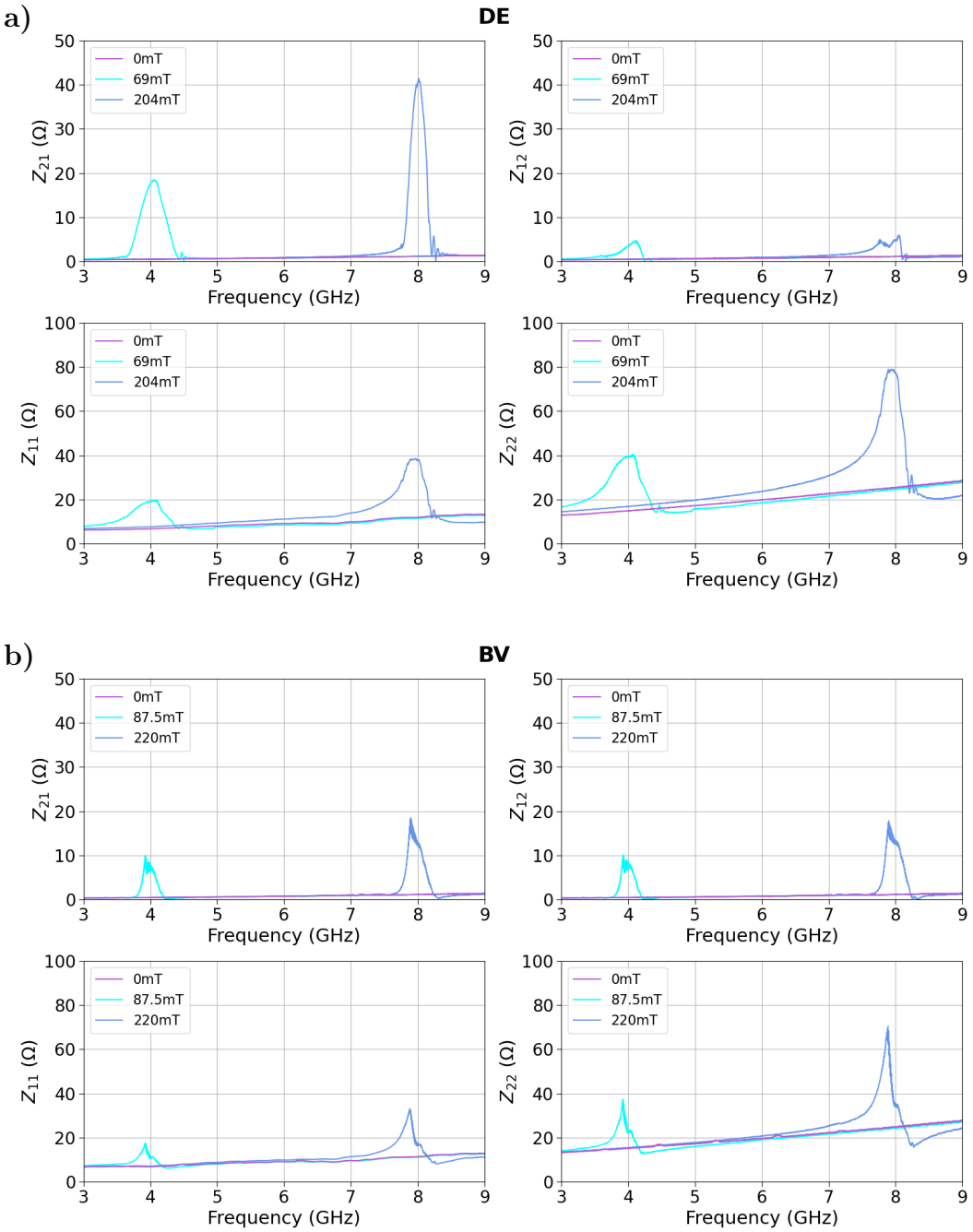

Figure 4.7: Impedance parameters calculated from the measured S-parameters using Eqs. 2.8 for a) DE and b) BV modes. The applied magnetic fields are indicated in the legend.

4.2.2 Impedance reconstruction

The measured S-parameters were then recalculated into the impedance Ω using Eqs. 2.8. The reconstructed impedances for the DE and BV modes are shown in Figure 4.7. The antenna impedances correspond to the peak values in the Z_{21} spectra. In the ideal case, the antenna impedance should be 50 Ω to ensure optimal matching with standard microwave systems. Upon examining the presented plots, the following observations were noted: for the DE mode, the impedance is consistently higher than for the BV mode. Additionally, both modes exhibit an increase in impedance at higher frequencies. Notable is the fact that the Z_{21} impedance for the DE mode around 8 GHz is higher than 40 Ω, approaching the ideal matching condition, while all the other impedances are below 20 Ω (see Fig. 4.7).

4.2.3 SW dispersion relation and antenna excitation efficiency

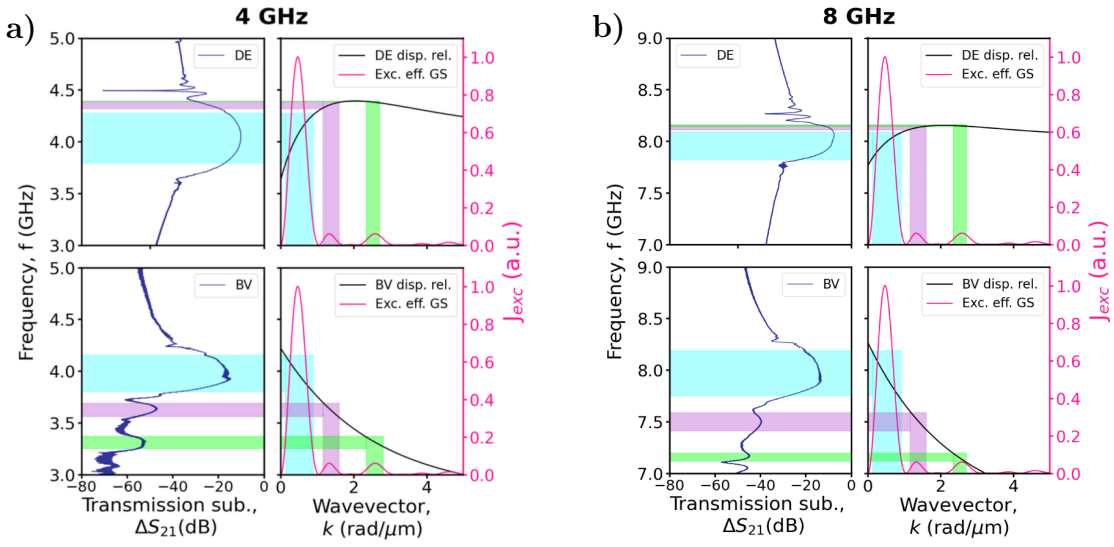

Figure 4.8: (left panels) SW transmission with subtracted background measured using 440 µm long GS antennas at an input power of -15 dBm at a) 4 GHz and b) 8 GHz for DE (upper panels) and BV modes (lower panels). (right panels) Calculated dispersion relation (black), antenna excitation efficiency (magenta) for a sample of thickness 802 nm. The dispersion relation was reconstructed using the Kalinikos-Slavin model [20] (see Eq. 1.27). The cross-sections of the dispersion relation and antenna excitation efficiency are highlighted in cyan, purple and green. The applied magnetic fields are depicted in Tab 4.2.

To further evaluate the efficiency of SW signal transmission at the nanoscale across the two distinct frequency ranges of 4 GHz and 8 GHz, Figure 4.2 is created. This figure displays the dispersion relation (black curve) and the antenna excitation efficiency J_{exc}

(magenta curve), alongside the spin wave transmission with subtracted background ΔS_{21}. The use of background-subtracted data provides a clearer depiction of the transmitted SW signal. The dispersion relation (black curve) was constructed using the Kalinikos Slavin model [20] (see Eq. 1.27), with the following input parameters: gyromagnetic ratio $\frac{\gamma}{2\pi} = 28\,\frac{\mathrm{GHz}}{\mathrm{T}}$, saturation magnetization $M_\mathrm{s} = 140\,\frac{\mathrm{kA}}{m}$, exchange constant $A_\mathrm{ex} = 3.6\,\frac{\mathrm{pJ}}{\mathrm{m}}$, and pinning conditions: fully pinned. For the calculation of the excitation efficiency of the used GS antennas fabricated on the YIG sample, the following equation was employed:

$$J_\mathrm{exc}(k) = \left| \frac{1}{ika} \left(e^{-ika} - 1\right) \left(e^{-ik(a+b)} - 1\right) \right|^2 \tag{4.3}$$

where a is the conductor's (ground and signal lines) width and b is the spacing between the signal and the ground line. For the used antennas $a = 3.6\,\mu\mathrm{m}$ and $b = 2.4\,\mu\mathrm{m}$ (see Fig. 2.2).

The bands highlighted in cyan, purple, and green in Fig. 4.2 mark the regions where the dispersion relation intersects with the antenna excitation efficiency. Ideally, each highlighted band should align with both a peak in the excitation efficiency spectrum and the corresponding peak in the SW transmission spectra. Thus, these regions define the frequency f and wavevector k ranges where spin waves are efficiently excited by the antenna and successfully propagate through the material.

5 Discussion

5.1 PSWS at the Macroscale

Spin wave-based power limiters are of crucial importance because they offer frequency-selective protection for RF components in modern communication systems from large incoming signals, by keeping the output power at a constant power limiting level after the power threshold [18]. One big advantage that ferrite spin wave-based power limiters have in comparison to conventional semiconductor-based limiters is that they can also operate at high frequencies (5G) without electronic noise causing a problem [4].

SW-devices enable multi-functionality within a single unit, simultaneously serving as power limiters, filters, and delay lines. This property makes them highly versatile for RF systems [4, 30]. By integrating all three functions into one device, space and energy are efficiently saved [4]. Such multi-functional SW devices can play a vital role in CMOS circuits. If these functions were to be implemented using traditional CMOS, each would require separate circuitry. Additionally, although CMOS technology has progressed toward nanoscale dimensions, fundamental physical and technical challenges have emerged that impede further miniaturization [32]. Unlike traditional CMOS circuits, where information is carried by electrical current, in SW devices, information propagates through oscillations in magnetization, which dramatically reduces energy loss due to Joule heating, and thus forms an advantage over CMOS circuits [2, 31, 32]. The ability of spin-wave devices to operate at high frequencies opens the door to functional device elements with dimensions well below the scaling limits of conventional CMOS transistors [31, 32]. Furthermore, studies indicate that, compared to conventional CMOS circuits, hybrid spin wave–CMOS computing systems may achieve significantly lower power consumption [32]. Thus, it can be anticipated that integrating such multi-functional SW devices with CMOS circuits could offer the possibility of highly miniaturized, energy-efficient, and reconfigurable signal processing systems in the future [32]. However, there still remain challenges to realize such hybrid spin-wave–CMOS computing systems [32]. It can not yet be claimed that magnonic logic devices will outperform scaled CMOS technology in all aspects [31].

5.2 PSWS at the Nanoscale

A critical challenge in nanoscale calibration is ensuring that all three conducting tips of the picoprobes make precise contact with the antenna pads on the YIG film. This proved to be problematic with the previous sample holder design, resulting in unsuccessful calibration attempts. The integration of goniometric stages, providing controlled pitch adjustment, into the new sample holder design effectively addresses this issue by allowing the tips

of the picoprobes to be accurately tilted and positioned onto the calibration structures. This enhancement ultimately made it possible to achieve a successful calibration for 50 Ω impedance matching between the antennas and the VNA.

Despite this successful calibration enabling the reconstruction of antenna impedances, Fig. 2.3 reveals that the measured impedances deviate from the ideal 50 Ω, generally remaining below 20 Ω, except for the impedance near 8 GHz in the DE mode. This discrepancy could be attributed to the fact that the physical impedance of the GS antennas used does not perfectly match 50 Ω. Since antenna impedance depends on geometric parameters such as the width and spacing of the ground and signal lines, even small deviations in these dimensions could alter the characteristic impedance. The antennas were fabricated on the YIG sample using electron beam lithography. Small variations in the conductor width during the fabrication process could result in deviation from the intended characteristic impedance of 50 Ω. Additionally, suboptimal contact between the picoprobe tips and the antenna contact pads may have contributed to the reduced impedance values. Although a source meter was employed to detect contact, it was challenging to reliably determine the exact moment the picoprobes made electrical contact, which inadvertently caused minor scratches on the contact pads and the calibration structures. This could have introduced additional parasitic effects. Finally, the deviation may also have resulted from the use of antennas that were too short.

Improving the impedance values to the desired 50 Ω could potentially be achieved by using longer antennas or by optimizing both the fabrication process of the antennas in the sample and the contacting procedure between the antennas and the picoprobes.

When further analyzing the antenna excitation efficiency and the dispersion relation constructed using the Kalinikos-Slavin model [20] for the DE mode at both frequency ranges (4 GHz and 8 GHz) in Figure 4.8, it is evident that the first peak in the antenna excitation spectrum corresponds well to the peak in the measured SW transmission spectrum. However, a discrepancy is apparent for the second and third peaks, highlighted by the purple and green bands. Here, neither the purple nor the green band fully encompasses the corresponding peak observed in the SW transmission spectrum. This mismatch may arise from the limitations of the Kalinikos-Slavin model used to reconstruct the dispersion relation, which, for YIG films as thick as $d = 802$ nm, is strictly valid only within the dipolar regime [20]. In contrast, for the BV mode, the agreement between excitation efficiency and transmission spectra is excellent for all three peaks, both at 4 GHz and 8 GHz (see Fig. 4.8).

In addition to using analytical models like the dipolar dispersion relation equation and the Kalinikos-Slavin model to reconstruct the SW dispersion relation (see Fig. 4.8), simulations were created using the dispersion calculator by the PhD student at the University of Vienna Andrey A. Voronov (see Figs. 5.1 and 5.2). This dispersion calculator uses the TetraX package for finite-element-method (FEM) micromagnetic modeling of magnetization statics and dynamics [42] to perform numerical calculation of SW dispersion curves for three different sample geometries and three distinct materials. The TetraX

package constructs spin wave dispersion relations using the FEM. This method numerically solves a plane-wave version of the linearized equation of motion of the magnetization and is designed to handle complex magnetic geometries. [42, 43]

To reconstruct the simulated dispersion relation with the dispersion calculator, the following parameters were defined: material parameters, geometry of the sample, applied external field, wavevector k range, and number of SW modes. The simulated dispersion curves and those obtained using the Kalinikos-Slavin model were generated for modes $n = 0$ - 5, whereas the analytical dipolar dispersion relation is plotted only for the fundamental mode $n = 0$ (see Figs. 5.1 and 5.2).

The comparison of three different methods to create the dispersion relation aims to analyze how the analytical models deviate from the simulation and which model best describes the measured SW transmission. Running these simulations alongside analytical treatments is essential to bridge the gap between simplified theoretical predictions and experimental observations.

Although both the dipolar dispersion relation and the Kalinikos-Slavin model provide valuable theoretical insights by describing SW dispersion based on established physical principles, they incorporate simplifying assumptions and approximations that constrain their accuracy in certain regimes. Specifically, the dipolar dispersion relation (Eqs. 1.29 and 1.30) is relatively simple and valid only for low wavevectors (dipolar regime) where exchange effects are negligible. This model ignores higher-order quantization effects or boundary conditions. In contrast, the Kalinikos-Slavin model (Eq. 1.27) extends accuracy to both the dipolar and the exchange regimes but shows significant limitations in the dipolar-exchange regime [20]. Compared to the two analytical models, the simulated dispersion curves (see fourth panel from the left in Figs. 5.1 and 5.2), generated using the dispersion calculator based on the TetraX package [42, 43], incorporate all interactions, which results in notable deviations in the dispersion curve shapes, particularly for the DE mode.

The greatest deviation between the analytical models and the simulated curves for the DE mode is observed for mode $n = 0$: The simulated dispersion curve is almost completely flat, while the analytical models show a fairly steep slope of the dispersion curve for wavevectors k between 0 rad/µm and 1 rad/µm (see Figs. 5.1 and 5.2). Concerning higher modes $n = 1$ - 5, the dispersion curves derived from the Kalinikos-Slavin model also exhibit a steeper slope across the entire k-range compared to the corresponding simulated curves. This difference is particularly pronounced for modes $n = 1$ - 3 (see Figs. 5.1 and 5.2).

The fact that the simulated dispersion curves are flat indicates low SW group velocity v_g. The individual modes $n = 0$ - 5 in the simulation can undergo hybridization, which means that different spin wave modes n interact and mix when their frequencies and wavevectors come close to each other. This results in the splitting or merging of modes instead of distinct, separate dispersion branches. After this hybridization, the modes effectively combine to form a single dispersion curve resembling the one predicted by the Kalinikos-Slavin model for the mode $n = 0$, which is smoother and has a prominent slope in certain regions.

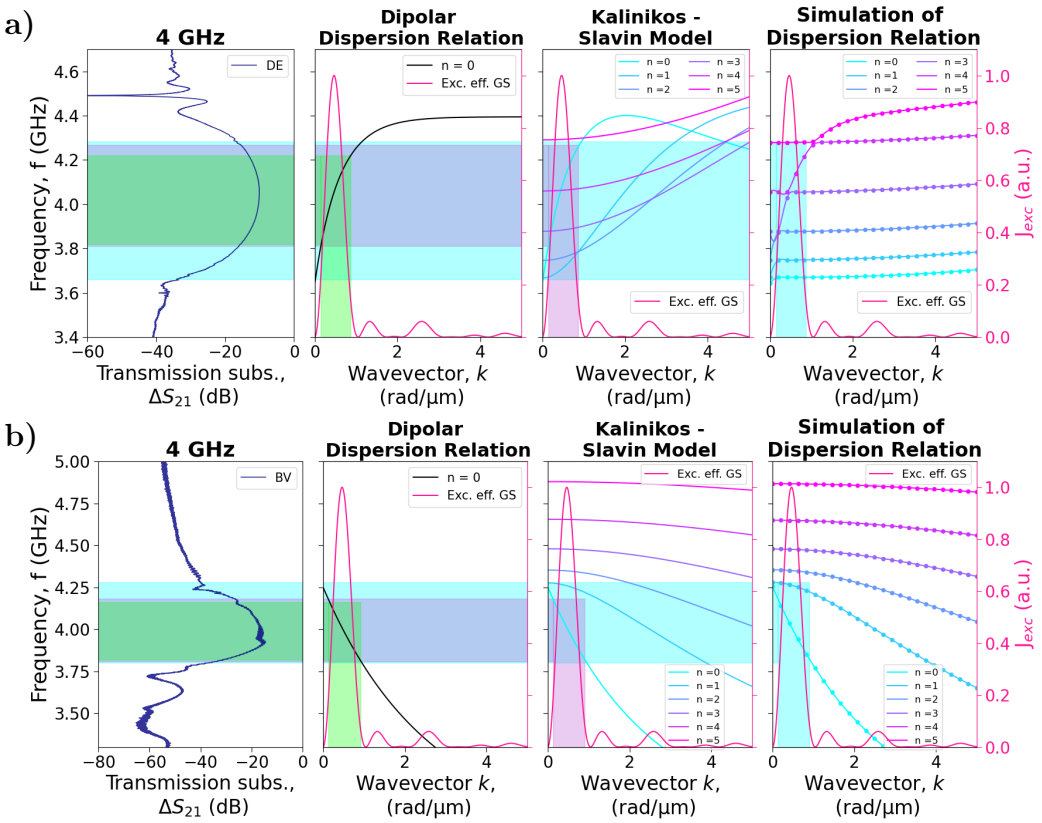

Figure 5.1: Comparison of analytical models of the SW dispersion relation with a simulation. (first panels from the left) SW transmission measured using 440 µm long GS antennas on a sample of thickness 802 nm, at an input power of -15 dBm at 4 GHz for both the a) DE mode (upper panels) at a magnetic field value of 69 mT and the b) BV mode (lower panels) at at a magnetic field value of 87.5 mT. (second panels from the left) Dispersion relation (black), reconstructed using the dipolar dispersion relation (see Eqs. 1.29 and 1.30), and antenna excitation efficiency (magenta). (third panel from the left) Dispersion relation for the modes $n = 0$ - 5, reconstructed using the Kalinikos-Slavin model [20] (see Eq. 1.27), and antenna excitation efficiency (magenta). (fourth panel from the left) Simulation of the SW dispersion relation for the modes $n = 0$ - 5, created using the dispersion calculator created by PhD student Andrey A. Voronov at the University of Vienna [42, 43]. The correspondence between the peak in the transmission spectrum and the peak in the antenna excitation efficiency is highlighted in cyan, violet and green.

When examining the DE mode in Figures 5.1 and 5.2, it is evident that for both frequency ranges (4 GHz and 8 GHz) the simulated model created by the dispersion calculator most accurately captures the transmitted SW signal. This is demonstrated by the cyan

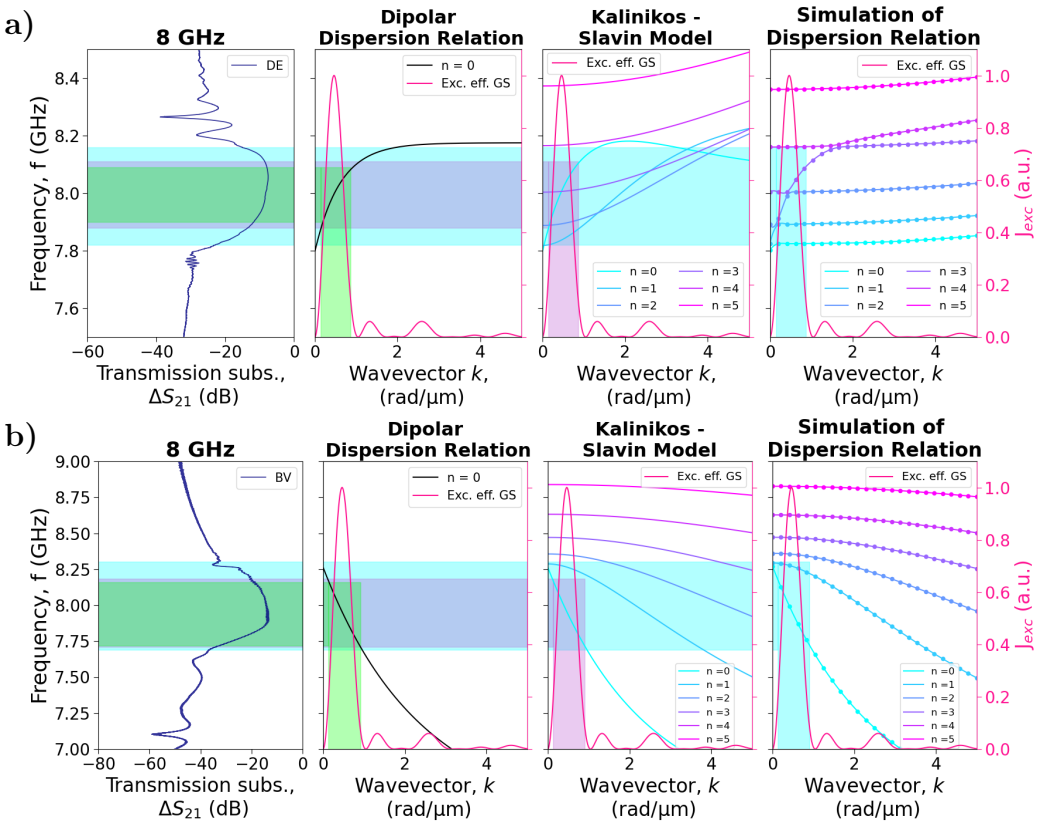

Figure 5.2: Comparison of analytical models of the SW dispersion relation with a simulation. (first panels from the left) SW transmission measured using 440 µm long GS antennas on a sample of thickness 802 nm, at an input power of -15 dBm at 8 GHz for both the a) DE mode (upper panels) at a magnetic filed of 204 mT and the b) BV mode (lower panels) at a magnetic field of 220 mT. (second panels from the left) Dispersion relation (black), reconstructed using the dipolar dispersion relation (see Eqs. 1.29 and 1.30), and antenna excitation efficiency (magenta). (third panel from the left) Dispersion relation for the modes $n = 0$ - 5, reconstructed using the Kalinikos-Slavin model [20] (see Eq. 1.27), and antenna excitation efficiency (magenta). (fourth panel from the left) Simulation of the SW dispersion relation for modes $n = 0$ - 5, created using the dispersion calculator created by PhD student Andrey A. Voronov at the University of Vienna [42, 43]. The correspondence between the peak in the transmission spectrum and the peak in the antenna excitation efficiency is highlighted in cyan, violet and green.

highlighted band, which covers the majority of the peak observed in the transmission spectrum (see first panel from the left in Figs. 5.1 and 5.2).

In contrast to the results for the DE mode, the BV mode exhibits consistent outcomes

across all three methods. At both frequency ranges (4 GHz and 8 GHz), the dispersion curves for mode $n = 0$, generated by the two analytical models and the simulation, closely match in shape (see Figs. 5.1 and 5.2). Consequently, all three approaches accurately describe the measured SW transmission, as highlighted by the shaded bands in the figures. Even for higher modes $n = 1$ - 5, the dispersion curves obtained from the Kalinikos-Slavin model remain in very good agreement with the simulated curves (see Figs. 5.1 and 5.2).

Conclusion

The present thesis has been dedicated to improving the experimental setup for the investigation of propagating spin waves at the nanoscale, by addressing critical challenges in the calibration of the VNA and the reconstruction of the antenna impedance. To improve the measurement setup, two new components were created: a sample holder optimized for in-plane measurements at the nanoscale and a stage for the optical microscope. The creation process included first the design of the two components in the software for 3D modeling of mechanical parts and assemblies, Autodesk Inventor, then the fabrication of the single parts at the workshop of the Department of Physics at the University of Vienna, and finally the assembly of the parts in the laboratory.

Through integrating goniometric stages into the new design of the sample holder, the calibration for a 50 Ω impedance matching between the microwave antennas and the VNA was achieved. The successful calibration, in turn, enabled the accurate reconstruction of antenna impedance for antenna performance analysis. Improving the antenna performance leads to better SW signal transmission. The custom stage for the optical microscope, on the other hand, was developed to provide a stable and adjustable platform, so that the microscope can be positioned precisely over the sample during measurements. This stage supports both in-plane and out-of-plane configurations, enhancing the experimental flexibility and accuracy when using the microscope to achieve accurate contact of the picoprobes with the antennas on the film.

Using Propagating Spin Wave Spectroscopy (PSWS), this thesis investigates spin wave transmission at both the macro- and nanoscale. To perform PSWS, a VNA was employed as the measurement system.

At the macroscale, experiments were conducted using a pair of 13 mm long stripline antennas, fabricated on YIG film of thickness 7.78 µm. The measurements involved both magnetic field and power sweeps and aimed to investigate the multifunctional capabilities of SW devices to operate simultaneously as frequency selective power limiters, delay lines, and RF filters. For this purpose, various plots were created: The spin wave transmission spectra (SW signal in the frequency domain) show the filtering ability of SW devices. These plots allow the extraction of important characteristics of RF filters, such as insertion loss, bandwidth, and dynamic range. The lowest IL was achieved for the DE mode at 4 GHz, with a value of (17.8 ± 0.1) dB. The dispersion relation and antenna excitation efficiency plots visualize the frequency and wavevector ranges where a spin wave was effectively excited by the antennas and transmitted through the material. These plots also include the SW group velocity, which was derived from the dispersion relation. The time-domain signal plots, created by applying Fourier transforms to the frequency-domain data, allow for a clear distinction of the pure spin wave contributions

from electromagnetic leakage, enabling the extraction of delay times associated with spin wave propagation. These plots demonstrate the implementation of spin wave devices as delay lines, where the slower group velocity of SW compared to electromagnetic waves results in a measurable time shift in signal arrival. Finally, the power transmission spectra illustrate a spin wave-based frequency-selective power limiter. The constructed power characteristics curves reveal the power threshold and corresponding power limiting level after which the output power remains constant due to magnon scattering effects. For the DE mode at 11.8 mT, the power threshold occurred at $P_{\mathrm{th}} = 25$ dBm, whereas at 89.5 mT, for the same mode, no threshold was observed within the studied input power range of -45 dBm to 5 dBm.

For nanoscale measurements, 440 µm long U-shaped GS antennas fabricated by e-beam lithography on a 802 nm thin YIG film were used. Here, the primary focus was to create a new sample holder and a stage for the optical microscope and test their abilities in calibrating the VNA, which is a necessary step for reconstructing the antenna impedance. Using the measured data, several key plots were generated: The SW transmission and reflection spectra, created from the measured S-parameters for the DE and BV modes, show the successful SW excitation and efficient propagation at two different frequency ranges (4 GHz and 8 GHz). The relatively low ILes of less than 15 dB, extracted from the transmission peaks, validate effective signal transmission. The lowest IL was achieved for the DE mode at 8 GHz, with a value of (8.2 ± 0.1) dB. The plots showing the reconstructed antenna impedance confirm the successful calibration of the system for a 50 Ω impedance matching between the GS antennas and the VNA, which was the main goal of the present thesis. The deviation of the calculated antenna impedance from the ideal 50 Ω demonstrated the impact of both antenna geometry and contact precision on the matching condition. Most importantly, these impedance values serve as valuable diagnostic tools for assessing and optimizing antenna performance, paving the way to achieve better spin wave transmission and reducing signal losses. In the final part of the nanoscale study, the spin wave dispersion relation was constructed and compared using three different approaches: the analytical dipolar dispersion relation model, the Kalinikos-Slavin model, and a simulation generated by the dispersion calculator. These dispersion curves were plotted together with the excitation efficiency of the GS antennas. Direct comparison enabled the verification of theoretical predictions and helped not only to identify the simulations of the dispersion curves as the method that most accurately describes the measured SW transmission but also to recognize discrepancies, which can arise from limitations in the analytical models.

Bibliography

[1] V. V. Kruglyak et al. Magnonics. *Journal of Physics D: Applied Physics, Volume 43, Number 26*, 2010.

[2] A. V. Chumak et al. Magnon spintronics. *Nature Physics, Volume 11, Issue 6, pp. 453-461*, 2015.

[3] Philipp Pirro. Spin wave logic: from boolean to neuromorphic computing. https://download.uni-mainz.de/fb08-spice/2018-10-08-SMN/SMN-2018-Pirro.pdf, 2018. Presentation, Fachbereich Physik and Landesforschungszentrum OPTIMAS, Technische Universität Kaiserslautern.

[4] Kristýna Davídková et al. Nanoscale spin-wave frequency-selective limiter for 5G technology. *Physical Review Journals*, 2025.

[5] A. Prabhakar & D. D. Stancil. *Spin Waves: Theory and Applications*. Springer, 2009.

[6] J. M. D. Coey. *Magnetism and Magnetic Materials*. Cambridge University Press, 2010.

[7] Kannan M. Krishnan. *Fundamentals and Applications of Magnetic Materials*. Oxford University Press, 2016.

[8] Arati G. Kolhatkar et al. Tuning the Magnetic Properties of Nanoparticles. *Int J Mol Sci.*, 2013.

[9] J.P. Lynch M.L. Wang and H. Sohn. *Sensor Technologies for Civil Infrastructures, olume 1: Sensing Hardware and Data Collection Methods for Performance Assessment*. Woodhead Publishing, 2014.

[10] Majid Montazer and Tina Harifi. *Nanofinishing of Textile Materials*. Woodhead Publishing, 2018.

[11] Wai Kai Chen. *The Electrical Engineering Handbook*. Academic Press, 2004.

[12] Ralph Skomski. *Simple Models of Magnetism*. Oxford University Press, 2008.

[13] Robert M. White. *Quantum Theory of Magnetism: Magnetic Properties of Materials*. Springer, 2007.

[14] Wikipedia. Landau–lifshitz–gilbert equation. https://en.wikipedia.org/wiki/Landau%E2%80%93Lifshitz%E2%80%93Gilbert_equation, 2025. Accessed: 2025-07-22.

[15] Nanomagnetism and Magnonics. Introduction to spin waves. https://www.youtube.com/watch?v=V5b48utfpMQ&t=1422s, 2020. YouTube video, accessed: 03/08/2025.

[16] Florian Ciubotaru. *Spin-wave excitation by nano-sized antennas*. PhD thesis, Technische Universität Kaiserslautern, 2012.

[17] P. E. Zil'berman et al. Excitation and propagation of exchange spin waves in films of yttrium iron garnet. *Journal of Experimental and Theoretical Physics*, 1995.

[18] Khrystyna O. Levchenko et al. Review on spin-wave RF applications. *arXiv*, 2024.

[19] Burkard Hillebrands. Spin wave resonance techniques. https://magnetism.eu/esm/2024/slides/esm2024-hillebrands-slides-2.pdf, 2024. Accessed: 2025-07-18.

[20] B. A. Kalinikos & A. N. Slavin. Theory of dipole-exchange spin wave spectrum for ferromagnetic films with mixed exchange boundary conditions. *Journal of Physics C: Solid State Physics*, 1986.

[21] Bradley D. Volkerts. *Yttrium: Compounds, Production and Applications*. Nova Science Pub Inc, 2011.

[22] Vladimir Cherepanov et al. The saga of YIG: Spectra, thermodynamics, interaction and relaxation of magnons in a complex magnet. *Elsevier B.V.*, 1993.

[23] Anastasia Golovin. All-electrical spin wave spectroscopy, 2019.

[24] Seo ongpyo et al. Tunable asymmetric spin wave excitation and propagation in a magnetic system with two rectangular blocks. *Scientific Reports*, 2021.

[25] Rohde & Schwarz. *RS ZNA Vector Network Analyzer Getting Started*, 2024. Accessed: 2025-07-23.

[26] Wikipedia. Network analyzer (electrical). https://en.m.wikipedia.org/wiki/Network_analyzer_(electrical), 2025. Accessed: 2025-07-23.

[27] Keysight Technologies. Network analysis. https://www.keysight.com/us/en/solutions/measurement-fundamentals/network-analysis.html, 2018. Accessed: 2025-07-23.

[28] Wikipedia. Electrical impedance. https://en.wikipedia.org/wiki/Electrical_impedance, 2025. Accessed: 2025-07-23.

[29] David M. Pozar. *Microwave Engineering, 4th Edition*. Wiley, 2011.

[30] A. V. Chumak et al. Magnonic crystals for data processing. *Journal of Physics D: Applied Physics, Volume 50, Number 24*, 2017.

[31] Alexander Khitun et al. Magnonic logic circuits. *Journal of Physics D: Applied Physics, Volume 43, Number 26*, 2010.

[32] Mahmoud Abdulqader et al. An Introduction to Spin Wave Computing. *Journal of Applied Physics*, 2020.

[33] Wikipedia. Fast fourier transform. https://en.wikipedia.org%/wiki/Fast_Fourier_transform, 2025. Accessed: 2025-06-25.

[34] T. Hula et al. Spin-wave frequency combs. *Applied Physics Letters*, 2022.

[35] WaveMetrics. Products- igor pro - data analysis - signal processing. https://www.wavemetrics.com/products/igorpro/dataanalysis/signalprocessing, 2025. Accessed: 2025-07-18.

[36] Stuart Watt and Mikhail Kostylev. Reservoir computing using a spin wave delay line active ring resonator. *Physical Review Journals*, 2020.

[37] Kun Xue & R.H. Victoria. High data rate spin-wave transmitter. *Scientific Reports 14*, 2024.

[38] Xingyu Du et al. Frequency tunable magnetostatic wave filters with zero static power magnetic biasing circuitry. *Nature Communications 15*, 2024.

[39] Yiyang Feng. *Advancements in Spin Wave Devices for Next-Generation Radio Frequency Technology*. PhD thesis, Purdue University, 2023.

[40] György Csaba et al. Perspectives of using spin waves for computing and signal processing. *Physics Letters A*, 2017.

[41] M. B. Jungfleisch et al. Thickness and power dependence of the spin-pumping effect in Y3Fe5O12/Pt heterostructures measured by the inverse spin Hall effect. *Physical Review Journals*, 2015.

[42] A. Hempel F. Zahn A. Otto E. Westphal R. Hertel A. Kakay Attila L. Körber, G. Quasebarth. TetraX: Finite-Element Micromagnetic-Modeling Package. https://doi.org/10.14278/rodare.1418, January 2022.

[43] A. Otto A. Kákay L. Körber, G. Quasebarth. Finite-element dynamic-matrix approach for spin-wave dispersions in magnonic waveguides with arbitrary cross section. *AIP Advances*, 11, 2021.

List of Abbreviations

BV Backward Volume. 13, 27–32, 35–38, 41, 43, 44, 47

BVMSW Backward Volume Magnetostatic Spin Waves. 14

BW bandwidth. 31, 32

DE Damon-Eshbach. 13, 27–32, 34–38, 41–44, 46, 47

FMR Ferromagnetic Resonance. , 9–11

FV Forward Volume. 13

FVMSW Forward Volume Magnetostatic Spin Waves. 14

IL insertion loss. 31, 32, 35, 46, 47

LL Landau-Lifshitz. 9, 10

LLG Landau-Lifshitz-Gilbert. 9

MSSW Magnetostatic Surface Spin Waves. 13, 14

PSSW Perpendicular Standing Spin Waves. 13

PSWS Propagating Spin Wave Spectroscopy. , 1, 2, 13, 16, 27, 35, 40, 46

RF radio frequency. 17, 31

S-parameters scattering parameters. 2, 18, 21, 36–38

SW spin wave. , 1–3, 9, 11–17, 23, 25, 27–33, 35, 38–47

VNA Vector Network Analyzer. , 1, 2, 16–20, 22, 23, 26, 27, 32, 35, 41, 46, 47

YIG Yttrium Iron Garnet. , 1–3, 6, 14, 15, 27, 28, 30, 32, 35, 36, 39, 46